Nonlinear electromagnetic stabilization of microturbulence by fast ions

UNIVERSITAT POLITÈCNICA
DE CATALUNYA
BARCELONATECH

Felipe Nathan de Oliveira Lopes

Department of Nuclear Science and Engineering
Polytechnic University of Catalonia

This dissertation is submitted for the degree of
Master in Nuclear Engineering

Barcelona School of Industrial
Engineering

August 2017

Acknowledgements

I would like to acknowledge the support given by my adviser, Mervi Mantsinen. She has always encouraged me to improve myself and has always given me the opportunities to do so. This research was supported by the Barcelona Supercomputing Center (BSC). I am grateful for the support and discussions with Hauke Doerk, which apart of the scientific discussions, shared with me newer and interesting points of view on some aspects of life. I also dedicate to my colleagues and professors from the Polytechnic University of Catalonia. I am also thankful to my colleagues Carles, Dani, Albert, and Xavi, from the Barcelona Supercomputing Center. We had plenty of joyful and pointless discussions, and I enjoyed each one of them. I thank colleagues from the Max Planck Institute for Plasma Physics who provided insight and expertise that greatly assisted the research.

I would also like to thank the Red Española de Supercomputación (RES) for allowing us to use their computational resource at the BSC. We are also grateful to the Marconi-Fusion and Helios supercomputers, for the time allocated to the completion of this research. I would like to thank also Fusenet for the financial support offered for the participation in the 21^{st} Transport Task Force Meeting to present the results of this work. A special thanks also go to the Argos scholarship, for their financial support. This work has been carried out within the framework of the EUROfusion Consortium and has received funding from the Euratom research and training programme 2014-2018 under grant agreement No 633053. The views and opinions expressed herein do not necessarily reflect those of the European Commission.

I would like to dedicate this work to my parents, Katia Aparecida and Gilson de Oliveira, and my brother, Yuri de Oliveira. They were always by my side in the moments when nothing made sense to me, and still are. For all the affection and attention they gave me, I will be eternally grateful. I dedicate it to my wife, Estel Villaronga, and her family, Imma, Bernart, Pau and Alba. Estel has entered in my life in a particular way and has always supported me. For some reason, she sees the meaning of things in life that I am not capable of seeing by myself. I dedicate it to my friends from my hometown, where I learned the concept of friendship. Specially to Caio and the "Bonde do Voyagem".

Publications and presentations

This MSc thesis is based on the work presented in the following papers and presentations.

[1] "Nonlinear electromagnetic stabilization of ITG microturbulence by ICRF-driven fast ions in ASDEX Upgrade". F.N. de Oliveira, H. Doerk, M .J. Mantsinen, C. Angioni, R. Bilato, Vl. Bobkov, D. Gallart, A. Gutiérrez-Milla, P. Mantica, T. Odstrčil,X. Sáez, G. Tardini and the ASDEX Upgrade and EUROfusion MST1 Teams. Paper and poster presented at the 44^{th} European Physical Conference on Plasma Physics. Belfast, Northern Ireland, June 2017.

[2] Best Poster Award at the PRACEdays17 conference for the poster "Nonlinear electromagnetic stabilization of ITG microturbulence by ICRF-driven fast ions in ASDEX Upgrade". F.N. de Oliveira, H. Doerk, M .J. Mantsinen, C. Angioni, R. Bilato, Vl. Bobkov, D. Gallart, A. Gutiérrez-Milla, P. Mantica, T. Odstrčil,X. Sáez, G. Tardini and the ASDEX Upgrade and EUROfusion MST1 Teams. Barcelona, Spain. May, 2017.

[3] "Stabilization of Microturbulence by Fast Ions in ASDEX Upgrade". F.N. de Oliveira, H. Doerk, M .J. Mantsinen, C. Angioni, R. Bilato, D. Gallart, A. Gutiérrez-Milla, P. Mantica, T. Odstrcil, X. Sáez, G. Tardini, and the ASDEX Upgrade and EUROfusion MST1 Teams. Extended abstract and poster presented at the 4th BSC Severo Ochoa doctoral symposium. Barcelona, Spain. May, 2017.

[4] "Modeling of ^{3}He minority heating and transport levels in AUG discharges with large core ion temperature gradient". M.J. Mantsinen, F.N. de Oliveira, H. Doerk, C. Angioni, R. Bilato, D. Gallart, A. Gutiérrez-Milla, P. Mantica, T. Odstrcil, X. Sáez, G. Tardini and the ASDEX Upgrade and EUROfusion MST1 Teams. Poster presented at the 21^{st} Joint EU-US Transport Task Force Meeting. Leysin, Switzerland. September, 2016.

[5] "Nonlinear electromagnetic stabilization of ITG microturbulence by ICRF-driven fast ions in ASDEX Upgrade". Invited talk to be presented at the 19th Transport and Confinement Topical Group Meeting of the International Tokamak Physics Activity (ITPA), 18-20 September, Helsinki, Finland.

The Master candidate carried out all of the simulations done with FIDO and GENE reported in this thesis and in the above publications and presentations. The work was carried out in close collaboration with Dr. Hauke Doerk under the supervision of Prof. Mervi Mantsinen within a large international scientific framework. The candidate had the main responsibility of preparing all the manuscripts above.

Abstract

In plasma physics, the specific aspect of the interaction between highly energetic ions and microturbulence is still an open problem and has a big impact on the plasma overall confinement quality. In the present work we investigate an experimental discharge where fast ions are thought to interact with the plasma and stabilize microturbulence activity, leading to an overall improvement of the plasma confinement on the ASDEX Upgrade tokamak. To quantify the impact of fast ions on the stabilization of Ion Temperature Gradient (ITG) microturbulence, and making use of state of the art codes GENE and FIDO, we simulate an experimental discharge in which high values of central ion temperature were measured. Due to the highly electromagnetic particularity of the discharges, a second class of instability is present, the Kinetic Ballooning Mode (KBM). Depending on the safety factor q, KBM instability can have a great impact on the final ion heat flux levels. Nonetheless, we find that fast ions have a pertinent impact on the reduction of ion heat flux for the discharges in consideration, and provide a microturbulence stabilizing mechanism.

Table of contents

List of figures **xi**

1 Introduction **1**
1.1 Motivation . . . 1
1.2 Closer look on nuclear fusion . . . 4
1.3 Confinement and heating . . . 5
1.3.1 Magnetic confinement fusion . . . 5
1.3.2 Ion cyclotron resonant heating . . . 8

2 The Experiment **11**
2.1 Introduction . . . 11
2.2 Experimental configuration . . . 12
2.3 Experimental results . . . 12

3 Transport and Gyrokinetic theory **15**
3.1 Dynamics in magnetized plasma . . . 15
3.2 Tokamak confinement . . . 17
3.2.1 Classical analysis . . . 17
3.3 Kinetic theory . . . 18
3.4 Transport theory . . . 19
3.4.1 Moments of Boltzmann equation . . . 19
3.4.2 Conserved quantities . . . 20
3.5 Neoclassical transport . . . 21
3.5.1 Random walk approach . . . 21
3.5.2 Neoclassical transport . . . 23
3.6 Turbulence and the Gyrokinetic theory . . . 25
3.6.1 Bohm diffusivity . . . 25
3.6.2 Turbulent mechanism . . . 25

3.6.3 Gyrokinetic approach . . . 26
3.6.4 Ballooning properties . . . 27
3.6.5 Fluxes . . . 28

4 Simulation codes **31**
4.1 GENE . . . 31
4.1.1 The equations . . . 33
4.1.2 Outputs . . . 35
4.2 FIDO . . . 37
4.2.1 Theoretical formalism . . . 37

5 Microturbulence stabilization **39**
5.1 FIDO analysis . . . 39
5.1.1 Results . . . 40
5.2 GENE analysis . . . 42
5.2.1 Linear results . . . 43
5.2.2 Nonlinear results . . . 45
5.2.3 Beyond dilution and stabilization . . . 49

6 Conclusion **51**

References **53**

Appendix A Moments of the Boltzmann equation **55**
A.1 Mass conservation . . . 55
A.2 Momentum conservation . . . 56
A.3 Energy conservation . . . 56

Appendix B Random walk approach coefficients **59**

Appendix C First approximation to neoclassical flux **61**

List of figures

1.1 Cross section for different fusion reactions [1]. 2
1.2 Simplified scheme of a tokamak. Figure courtesy of Max-Planck Institute for Plasma Physics. 3
1.3 Binding energy for different isotopes. 4
1.4 Schematic of a Torus. The blue arrow represents the toroidal direction and red the poloidal direction. 6
1.5 Cross section view of the ITER. Figure courtesy of iter.org. 7
1.6 Magnetic field generated by a central solenoid [2]. Here we can see how the change in magnetic field strength allow us to change the resonance location and heat the plasma in different positions. 9

2.1 Ion temperature in radial direction. Discharge 31555 with NBI only, 31562 ICRH off-axis, and 31563 with central ICRH. $\rho_{pol} \approx r/a$ where r/a is the normalized plasma minor radius [3]. 13

3.1 Diffusivity as function of collisionality regime. 24
3.2 Dissipation pathways within turbulent framework [4]. 26

4.1 Global GENE simulation of AUG reactor. Figure courtesy of genecode.org 32

5.1 Radial profile of power density transferred from ^{3}He ions to bulk ions. . . . 40
5.2 Radial profile of power density transferred from ^{3}He ions to electrons. . . . 41
5.3 Pressure profile of ^{3}He ions. 41
5.4 Spectral analysis and safety factor sensitivity scan for discharge 31562. . . 43
5.5 Spectral analysis and safety factor scan for discharge 31563. 44
5.6 Instability growth rate for a case with (green) and without (red) electromagnetic activity for discharge 31562. 44
5.7 Instability growth rate for a case with (green) and without (red) electromagnetic activity for discharge 31563. 45

5.8 Instability growth rate for a case with and without fast ions for discharge 31563. 45
5.9 The electric potential fluctuation levels for the case without fast ions of discharge 31563 in the x and y plane. 46
5.10 The electric potential fluctuation levels for the fast ions case of discharge 31563 in the x and y plane. 47
5.11 Ion heat flux simulation for discharge 31563, the read horizontal line represents the experimental ion heat flux. The time is expressed in terms of GENE normalized units, which is approximately one microsecond. 48
5.12 The ion heat flux level for the simulation with fast ions is smaller than that in Fig 5.11, which is an indication of the stabilization of fast ions. The time is expressed in terms of GENE normalized units. The whole time interval corresponds to approximately one microsecond. 49

Chapter 1

Introduction

1.1 Motivation

The increasing energy consumption has arrived to levels where the present energy sources are not going to be able to supply the energy demand for longer than some decades. The urgency of finding a new virtually endless source is obvious. On one hand, the issues faced by nuclear fission are mainly due to nuclear waste. Even though they are properly managed nowadays, they still generate discomfort for the general public. On another hand, renewable energy is a good solution at short time, but must be used in a good balance with a constant and abundant energy source.

In order to cope with this issues, nuclear fusion was proposed as an alternative, clean and endless energy source. It heats a gas of light atomic nuclei to temperatures in which the nucleus are close enough to overcome the Coulomb repulsion, creating heavier element and releasing energy.

To maximize the effective cross section, the most effective elements used are the Deuterium, ${}^{2}_{1}\mathrm{H}$, and the Tritium, ${}^{3}_{1}\mathrm{H}$, as seen in figure 1.1.

The reaction is described as

$$ {}^{2}_{1}\mathrm{H} + {}^{3}_{1}\mathrm{H} \rightarrow {}^{4}_{2}\mathrm{He} + {}^{1}_{0}\mathrm{n} + 17.59\mathrm{MeV}, \tag{1.1} $$

where the reaction gives origin to an alpha particle ${}^{4}_{2}\mathrm{He}$ and a neutron.

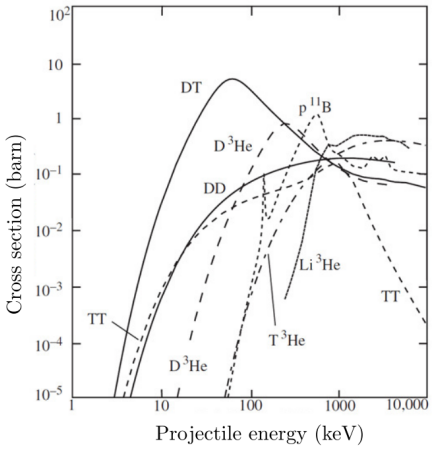

Fig. 1.1 Cross section for different fusion reactions [1].

In the case of heavenly bodies like stars with the mass of the sun or less, where nuclear fusion also takes place, it is important to notice that the main chain of fusion reaction of such bodies is the proton-proton chain reaction. That is due to the high pressure and density achieve in the center of such bodies. This reaction is described by the following equation,

$$ {}^{1}_{1}\mathrm{H} + {}^{1}_{1}\mathrm{H} \rightarrow {}^{2}_{2}\mathrm{He} + \gamma \rightarrow {}^{2}_{1}\mathrm{H} + \mathrm{e}^{+} + \nu_e + 0.42\mathrm{MeV}. \tag{1.2} $$

As we can see in the right hand side of equation 1.2, after the fusion reaction takes place, the ${}^{2}_{2}$He decays into ${}^{2}_{1}$H, plus an electron and an electronic neutrino.

It is necessary to remember also that, due to the large mass, the gravitational pressure of the sun is sufficient to keep the heated gas confined, and high values of kinetic energy are achieved by the protons. In the case of earthly nuclear fusion, the most common approach is using magnetic fields, and instead of the proton-proton reaction, a reaction with Deuterium and Tritium is chosen due to its higher cross section and higher values of energy released, as seen in equation 1.1.

Since the ionized heated gas is composed of different charged particles, it can be confined with strong magnetic fields in torus shaped devices such as tokamak or a stellarator. In the present work we are going to focus in the tokamak. The simplified scheme of this device is given in figure 1.2.

When considering the tokamak approach, one deals with a series of issues, mainly related to engineering capabilities to confine the plasma until it reaches ignition. Ignition is the point

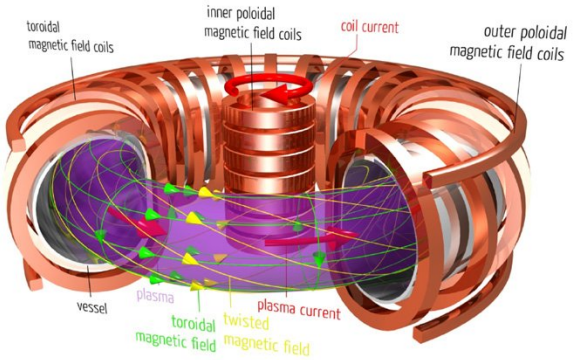

Fig. 1.2 Simplified scheme of a tokamak. Figure courtesy of Max-Planck Institute for Plasma Physics.

where the heat from the fusion reactions is enough to maintain the reaction ongoing without external input. After ignition, the reaction becomes self-sustaining, and no input power is required for the plasma burn.

In order to reach ignition, the plasma must be confined for a long period of time, and one of the main factor for the low plasma confinement time is the release of heat to the outside of the plasma environment. Transport of particles and heat is mainly produced by microturbulence, which is the focus of the present work. More specifically, we are going to understand how one could improve the quality of the plasma confinement by external means. To better understand how the stabilization of specific turbulent modes can be done, we review relevant basic plasma physics, as well as the characteristics of the tokamak device. The final aim of this work is to understand the impact of the presence of fast ions, generated by an external heating system, in the transport of particle and heat on the plasma. It is important to emphasize that fusion-born alpha particles occur naturally in an ignited plasma, as seen in equation 1.1, making the study of the effect of fast particles important.

A plasma is a state of matter in which a the electrons from the atoms are pushed apart, generating a gas of electrically charged particles. Transport is the mechanism in which mass, energy and momentum are exchanged in a given system, such as a plasma. In magnetically confined plasmas, non intuitive effects may appear due to the complexity of the interaction of the different particles with the background field and from the field with the particles. This topic will be further explained in chapter 3.

1.2 Closer look on nuclear fusion

In 1932, Ernest Rutherford discovered that lithium atoms, when split by protons, could release energy, in agreement with the mass-energy equivalence principle established by Albert Einstein. The discovery of the neutron by James Chadwick opened a path to what is known as the atomic era, where the nuclear energy was used as an alternative form of electric energy and as a novel weaponry mechanism.

Nuclear energy is considered as all the energy that is provided by the break down or fusion of nuclear particles [5]. Two approaches are known, the one involving the breakdown of heavy atom, known as nuclear fission and another one associated with the fusion of light nuclei, known as nuclear fusion. In the present work, we are going to focus on processes arising from the latter approach.

Figure 1.3 shows the different nature of the binding energy for different atomic numbers. It is seen that the energy released per nucleon in the case of fusion reactions is larger than the energy released in the fission case.

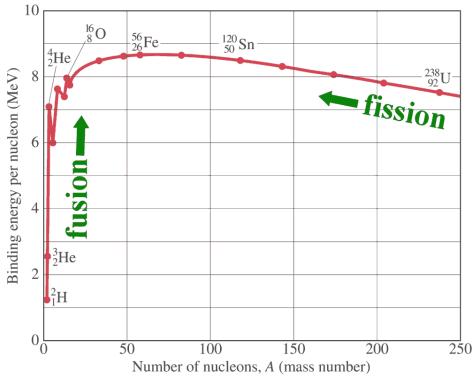

Fig. 1.3 Binding energy for different isotopes.

From the reaction 1.1, 17.59 MeV is released as energy. The essential point of the nuclear fusion is that Deuterium is found in sea water, in the form of heavy water, and the Tritium is bred in the nuclear reactor itself. It makes therefore the reaction cheaper and more abundant. In order for nuclei to fuse, they must be put close enough to overcome the electrostatic Coulomb potential. This means a certain amount of energy must be deposited on the system in order to achieve what is known as ignition.

1.3 Confinement and heating

An important concept in the field of nuclear fusion is the Lawson Criteria. It defines the condition between the plasma electron density n_e, the energy confinement time τ_E, and the plasma temperature for which we can have ignition. The equation represents a power balance in thermonuclear reactors in order reach a self sustained state in which no input of energy is required.

In the case of the Deuterium-Tritium reaction, for temperatures of the order of $T = 14keV$, the triplet product [6] is expressed by

$$nT\tau_E \geq 3 \cdot 10^{21} \mathrm{KeV} s/m^3. \tag{1.3}$$

Here, n is the density, T is the temperature and τ_E is the confinement time. The Lawson criteria is used as a guide to estimate required values of temperature to reach ignition for a given density n_e and energy confinement time τ_E.

Some concern must be addressed to the plasma confinement, and for how long its plasma facing components will cope with high heat load. The motivation of the present work is to find the best way to stabilize microinstabilities. Microinstabilities are small scales instabilities that take place in the plasma as means to release energy from large scales to small ones. We will have a closer look in the confinement and plasma heating method used.

1.3.1 Magnetic confinement fusion

Within the Magnetic Confinement Fusion (MCF) approach, different designs are often used. Magnetic mirrors pursue the confinement by means of the mirror effect of magnetic fields and the formation of magnetic bottles, structures formed when two diverging magnetic fields are put together. The main problem with this MCF approach is the edge physics, i. e. how the plasma can be contained in the beginning and end of the device. In order to solve this problem, a configuration in which the circular ends of the cylinder are joined together was proposed as a solution.

In topology theory, a Torus, schematically shown in 1.4, is a three dimensional surface obtained by the revolving of a circle around a co-planar axis. When used to mold the shape of the plasma where the nuclear fusion reactions are taking place, the torus shape presents

the advantage of allowing the magnetic field to have a toroidal geometry. Following the Poincaré–Hopf theorem of differential topology [7] and the Hairy Ball theorem of algebraic topology and its implications in topological properties of n-dimensional folds, the torus is a surface which possesses an Euler characteristic number equal to zero. It means we can drawn a continuous vector field in its surface with non vanishing points. It is important to fulfill this criteria because the magnetic field formed in this shape cannot have any vanishing point, since it would lead the plasma material to be thrown out of the system.

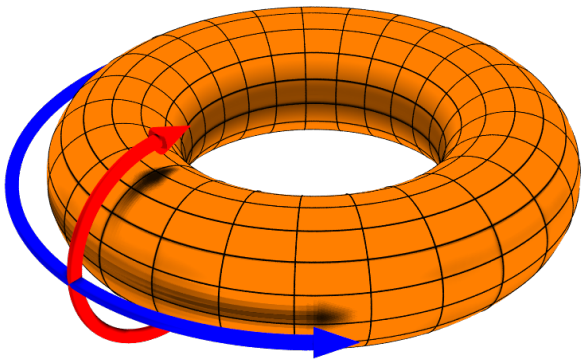

Fig. 1.4 Schematic of a Torus. The blue arrow represents the toroidal direction and red the poloidal direction.

Two main concepts are studied. The Stellarator, first proposed by Lyman Spitzer in 1950, is a toroidal device in which the non azimuth symmetric magnetic field is twisted in order to avoid drift losses to the containment. When toroidally confined, one of the problems that occurs with the plasma dynamics is that, due to the change in the magnetic field intensity inside and outside of the torus, a magnetic field gradient is generated. The plasma then tends to drift in a direction perpendicular to the magnetic axis and the centrifugal direction, and the reaction is terminated due to plasma losses. In the two proposed models, this issue is avoided due to the twisting of the magnetic field lines.

A solution to the drift problem is to bend the axial magnetic field lines in a poloidal direction, as illustrated by the red line in figure 1.4. In this way, the field lines create a flux surface around the whole torus, and a counteraction is generated in order to avoid the drift

losses. This approach is applied in Tokamak reactors.

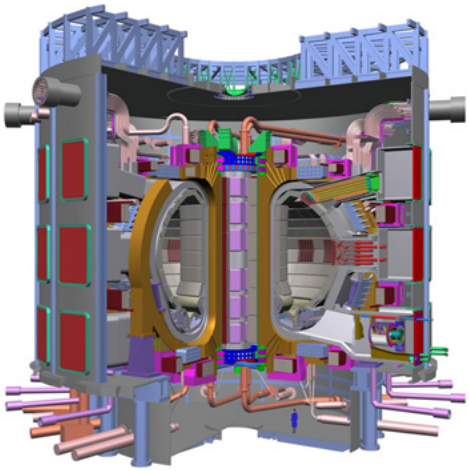

Fig. 1.5 Cross section view of the ITER. Figure courtesy of iter.org.

Tokamak is the Russian acronym of the "***to****roidal* ***ch****amber with* ***ma****gnetic* ***c****oils*". The first prototype was proposed by Lev Artsimovich in 1956. The tokamak is today the leading candidate design to reach the ignition and future economic feasibility in nuclear fusion. By using magnetic coils around the torus chamber, a toroidal magnetic field is generated in order to maintain the plasma confined. A second magnetic field, in the poloidal direction, is generated in order to bend the magnetic field lines, avoiding the magnetic gradient drift generated by the toroidal shape of the field. The latter field is generated by inducing a current in the plasma itself, following the principle of the Z pinch machine.

After laser scattering measurements, and with the confirmation of the higher temperatures and stability of the tokamak model, the tokamak fast became the most used confinement approach around the world. The ITER, latin for "*the way*", as shown in figure 1.5, started to be assembled in 2015. It is the world largest MCF device. It is expected to demonstrate an amplification of the input power of the order of 10 by the end of 2030 [8], showing the feasibility of nuclear fusion.

The first ITER heating mechanism is based on internal heating provided by the plasma current. This heating, known as ohmic heating, is also one of the main causes of plasma instability [9]. These instabilities are of Magnetohydrodynamic (MHD) nature. These MHD modes degrade the confinement and can lead to plasma disruption. Another unstable modes are microturbulent driven instabilities, which also degrade the confinement by facilitating high heat release and in consequence the decrease of confinement performance. The current

driven in the plasma increases its resistivity to values in which the Joule effect, used to heat the particles by friction, loses its effectiveness.

Apart of the ohmic heating due to current driven, ITER also uses three external heating mechanisms to heat the plasma. Neutral Beam Injection (NBI) is a system that injects neutral particles in the plasma in order to heat it by direct collisions. Electron Cyclotron Resonant Heating (ECRH) launches electromagnetic waves in the plasma in order to heat electrons by what is known as cyclotron heating. It is based on a process in which the particle acquires energy due to the fact that its magnetic resonant frequency is in phase with the resonance of the electric field of the electromagnetic wave launched at the plasma. A third method of plasma heating is Ion Cyclotron Resonant Heating (ICRH), discussed in more detail in the next section.

1.3.2 Ion cyclotron resonant heating

The central solenoid present in the tokamak reactor produces a magnetic field that decays inversely proportional to the distance to its main axis. It generates a magnetic field inside the plasma with ions resonating with a characteristic ion cyclotron frequency

$$\omega_{c,i} = \frac{q_i B}{m_i}, \tag{1.4}$$

where q_i and m_i are the charge and mass of the respective species. A more detailed description of the cyclotron motion is given in chapter 3, where the theoretical aspects of the present research are outlined. In this conjuncture, an electromagnetic wave with a frequency $\omega_{c,i}$, or its harmonic $n\omega_{c,i}$, tuned to ion cyclotron frequency allows us to heat a specific species in a specific position inside the plasma torus. This scheme is described as Ion Cyclotron Resonance Heating, .

As we can observe in the figure 1.6, the difference in the magnetic field strength at different positions generate an anisotropy in the profile, diminishing its strength in the direction outwards the solenoid axis. It allows for the tunning of the resonant location to heat it in different positions. It is important to realize that, due to collision with the main heated species, other ions present in the plasma can be heated indirectly by specific population heated by the ICRH mechanisms.

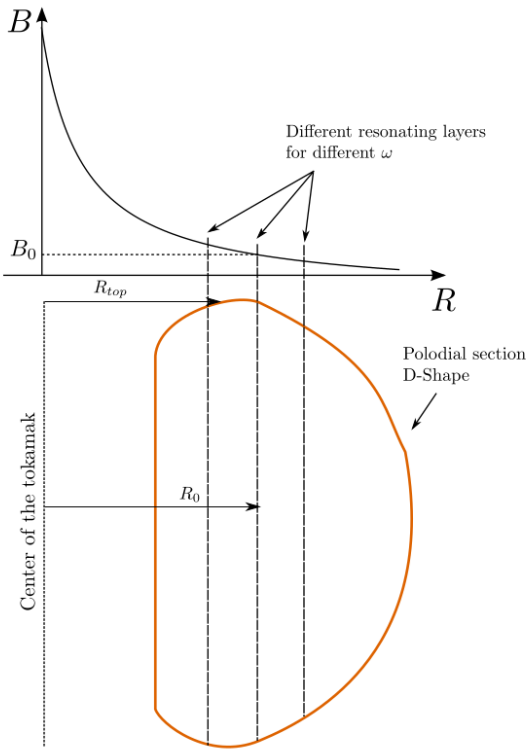

Fig. 1.6 Magnetic field generated by a central solenoid [2]. Here we can see how the change in magnetic field strength allow us to change the resonance location and heat the plasma in different positions.

The ICRH system is assembled in a way in which a generator produces high-power radio frequency waves that are transported in a transmission line and are, then, launched into the plasma through an antenna. The whole process is a highly complicated engineering endeavour, and problems with heating and wave leakage can damage the deposition performance and, therefore, degrade the heating of the plasma.

It is important to study the properties of ICRH because of its effects on the ion species. The electric part of the launched electromagnetic wave has two components with respect to the direction of the background magnetic field. The perpendicular component can be divided in left and right circularly polarized. The left polarization rotates in the direction of the ion rotation. We observe the appearance of a net acceleration, which is mainly due to the left polarized component. This increase in energy generates a high energy tail during the heating process. This process is responsible for the generation of fast ions.

Fast ions, although representing a small fraction of the total plasma density, are responsible for carrying up to one third of the total energy in reactors like ITER [8]. They can be born from ICRH and also as alpha particle from fusion reactions and NBI injection, explaining the importance of a good understanding of their properties. Fast ions have a trapped or passing orbit. In a passing orbit, they freely travel around the torus and lose their energy due to interaction with another species, meanwhile a trapped orbit will travel inside an specific closed orbit, known as banana orbit. Fast ions are reported [10] [11] to have an impact on the stabilization of microturbulence.

Reference [10] reports the stabilization of microturbulence in a discharge of JET tokamak, in United Kingdom. It analyses the different linear and nonlinear effects that fast ions can have in the stabilization of microturbulence process. Reference [11] focuses on the formation of Ion Transport Barriers in ASDEX Upgrade, Germany. In this work, the focus is given on the dilution stabilization, which will be discussed in detail in chapter 5. In the present work, we analyze a case beyond dilution, different of reference [11], and we analyze a discharge from the ASDEX Upgrade tokamak, not the JET tokamak as in case [10].

As we will describe with more detail in chapter 3, the objective of the present work is to investigate whether stabilization of microturbulences due to IRCcan be responsible for the high values of central ion temperature for the experimental discharges described in the chapter 2.

This thesis is divided in six parts. In the first part we have the introduction and motivation, described in the present chapter. The second chapter exposes briefly the experimental set up of the cases analyzed, and the fourth chapter discusses the numerical tools used. In the third chapter we discuss the theoretical background needed for the understanding of plasma transport and the origin of microturbulence, as well as the numerical applicability. In the fifth chapter the results are exposed, followed by the discussion, ending with the conclusions in the sixth chapter.

Chapter 2

The Experiment

In order to understand the effect of ICRH-driven fast particles in the stabilization of different types of microturbulence, we analyze an experiment in which a central ICRH deposition is employed, and a high value of central ion temperature is measured. We review the experimental set up as reported in [3], in order to comprehend the characteristics of the fast particles and how they affect the main ion temperature and other properties of the plasma.

2.1 Introduction

The use of ICRH waves to heat plasma is well known and it is one of the foreseen heating systems for ITER. As the only scheme capable of provide dominant bulk ion heating, it also facilitates control during the initial phase and assist the formation of H-mode. The H-modes are of great importance because it ensures a larger concentration of power inside the plasma, with a greater pressure gradient close to the edge.

In the ICRH scheme, the minority resonating species absorb the energy from the electromagnetic wave through ion cyclotron absorption, and then transfers this energy to the main ions through collision. In order to obtain predominant bulk ion heating, a high energy tail developed due to ion cyclotron damping needs to be reduced to a critical value described by the following

$$E_{critic} \approx 14.8 A T_e \left(\sum_j \frac{n_j Z_j^2}{n_e A_j} \right)^{2/3} . \tag{2.1}$$

At E_{critic} the total energy of a fast ion is equally distributed between electrons and ions. In 2.1, n_j, Z_j, A_j is the density, charge number and mass number of the ion species j. T_e

and n_e are the electron temperature and density, and A is the fast ion mass number. At low densities, the energy tail of fast ions tends to be larger, and we lose efficiency in the bulk heating of the main ion.

2.2 Experimental configuration

The two discharges under consideration were carried out in a H-mode deuterium plasma at the ASDEX Upgrade tokamak [3]. With a magnetic field of 2.8T and 3.0T, 3.5 MW of ICRH power was applied at a frequency of 30 MHz, generating the resonance position in the plasma core. NBI of deuterium at 4.5-6.5 MW was used as preheating. Discharge 31555 has only NBI as power source, this is the reference discharge. Meanwhile discharge 31562 has an off-axis ICRH deposition, and 31563 has a central ICRH deposition.

The ^{3}He is injected from a puff injection in the mid plane. The concentration with respect to electron concentration is below 5%. To measure the ion temperature and other parameters such as toroidal rotation, charge exchange recombination spectroscopy (CXSR) was used. With the use of Fourier analysis, the ions temperature was studied with respect to the ICRH power modulation. The electron temperature was measured with the Thomson scattering diagnostic.

2.3 Experimental results

An increase of almost 80% in central ion temperature was detected in discharge 31563 if compared to the reference discharge 31555. The reference discharge is heated with NBI power only. The electron temperature among the discharges was observed to increase from 2.5keV for 31555 to 3keV in discharge 31563.

Figure 2.1 shows the ion temperature profile for the discharges under consideration at $t = 3s$ in the discharge. With a central ICRH heating, more peaked values of central T_i is seen for the case 31563 if compared to the off-axis discharge 31562. In both cases, a significant increase is seen as compared to the reference discharge 31555.

The ion temperature profiles for discharge 31563 have a radial gradient of almost 50 keV/m and a normalized logarithmic ion temperature gradient R/L_{Ti} of 20. Those are large

values for an ASDEX Upgrade discharge.

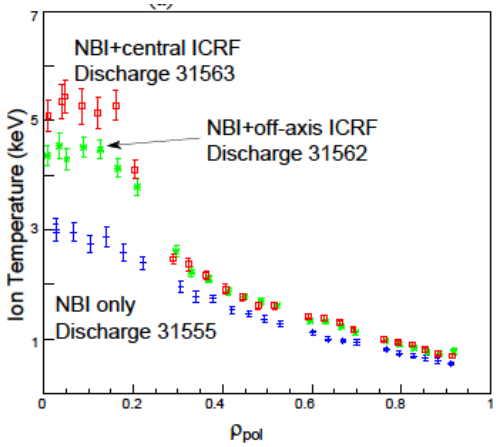

Fig. 2.1 Ion temperature in radial direction. Discharge 31555 with NBI only, 31562 ICRH off-axis, and 31563 with central ICRH. $\rho_{pol} \approx r/a$ where r/a is the normalized plasma minor radius [3].

Apart of the changes in the ion and electron temperature, an increase in plasma toroidal rotation was also observed, as well as Magnetohydrodynamics (MHD) activity. When ICRH is added, an increase in the toroidal rotation is observed for both central and off-axis discharges, even though no net torque is applied by the ICRH antennas.

The changes in MHD activity and toroidal rotation indicate changes in the plasma transport characteristics. This makes the assessment of bulk ion heating rather complicated, since high central radiation losses due to impurity accumulation could have an impact in the transport and therefore in the measured T_i.

The ICRH modeling with the TORIC code [12] give a bulk ion heating fraction of 56-80% for discharge 31563 and and the PION [13] give a value of bulk ion heating fraction of 70-80% for discharge 31563. Simulations of discharge 31563 carried out with PION also give the power transfer profiles from ICRH waves to the bulk ions. The heating profiles are peaked around the resonance near the plasma center, with a 0.4 MW/m^3 of power density for ions.

A possible explanation for the peaked ion temperature is the fast ion stabilization of ion temperature gradient turbulence [14] [15]. This hypothesis was suggested by reference [3]. The objective of the present work is to investigate if this suggestion holds from a transport

analysis point of view. In order to do so, in the next chapter we are going to have a brief introduction to relevant topics in transport theory.

Chapter 3

Transport and Gyrokinetic theory

As discussed in chapter 1, the plasma consists of ions and electrons, forming a *quasi-neutral* fluid. The fact that the plasma does not allow macroscopic charge separation does not mean that there are no electrostatic fields present. In most of the cases a property known as self-organization, vastly present in magnetized fusion plasma, allows the appearance of structures carrying significantly high values of electric fields [16], and therefore energy.

In the present chapter, we are going to understand how the different interactions are linked in the plasma physics of fusion reactions in order to better understand the theoretical framework that allows for the stabilization. More specifically, we are interested in fast particles that interact with the plasma, and change the plasma transport properties. To better understand how this interaction takes place, we review some aspects of the transport theory. It is important to have in mind that up to the day of the presentation of this work, there is no nonlinear theoretical explanation for the fast ion stabilizing effects. A detailed discussion about the nonlinear analyses is made in chapter 4.

3.1 Dynamics in magnetized plasma

In order to understand the dynamics of plasma toroidal confinement, one must first recall the dynamics of particles orbit under the influence of electric and magnetic fields. The *orbit theory* is used to study the dynamics of charged particles under the influence of electric and magnetic fields. The Hamiltonian mechanism is used in order to describe the dynamics of the system in the space of the canonical coordinates and it can be used to describe the conservation of a property known as adiabatic invariant.

Consider the Lorentz equation for a particle with charge **q** under the action of a force $\vec{F}$ due to the electric and magnetic fields $\vec{E}$ and $\vec{B}$, the movement of a particle can be described as

$$r(t) = \frac{1}{2}(\frac{\mathbf{q}E}{m})t^2 + v_0 t + r_0, \tag{3.1}$$

where r_0 is the initial position and v_0 is the initial velocity, with constant acceleration $\frac{\mathbf{q}E}{m}$. For a magnetostatic field the trajectory is found by separating the velocity of the particle in parallel and the perpendicular direction with respect to the background magnetic field. The movement in the direction of the magnetic field is not affected, and the perpendicular component of the resulting velocity is

$$\frac{dv_\perp}{dt} = \frac{q}{m}(v_\perp \times B), \tag{3.2}$$

considering $\Omega_c = -\frac{qB}{m}$, and considering that Ω_c is constant in a constant magnetic field, known as cyclotron frequency. Integrating 3.2 we have

$$v_\perp = \Omega_c \times r_c, \tag{3.3}$$

where $\vec{r}_c$ is the the particle position related to the center of the gyration point, in a plane perpendicular to $\vec{B}$. Equation 3.3 represents the rotation of the position $\vec{r}_c$. The resulting motion of the particle is given by the superposition of the uniform motion along $\vec{B}$ and the circular motion perpendicular to $\vec{B}$. The radius in which the particle gyro-rotates is known as Larmor radius, defined as $\rho = \frac{mv_\perp}{qB}$.

By separating the components of $\vec{v}$ and $\vec{E}$ parallel and perpendicular to $\vec{B}$ in the same direction of the magnetic field, we have

$$r_\parallel(t) = \frac{1}{2}(\frac{\mathbf{q}E_\parallel}{m})t^2 + v_\parallel(0)t + r_\parallel(0). \tag{3.4}$$

The perpendicular solution is found by separating $v(t)$ in $v\prime(t) + v_E$, being v_E a velocity in the plane perpendicular to B.

The final particle motion is described as

$$v(t) = \Omega_c \times r_c + \frac{E_\perp \times B}{B^2} + \frac{\mathbf{q}E_\parallel}{m}t + v_\parallel(0). \tag{3.5}$$

When E and B are perpendicular in a confined plasma, the second term on right hand side of equation 3.5, generates the $E \times B$ drift drift.

3.2 Tokamak confinement

Toroidal confinement is the configuration to which most of the manpower is devoted. Classical motion of particles in non uniform magnetic fields and the equilibrium of forces in a toroidaly magnetized plasma are of great importance in this configuration, and are concisely studied in this section.

3.2.1 Classical analysis

An important consideration must be done regarding the drift in slowly changing fields. In the case of a toroidally confined plasma, the geometry of the magnetic field allow it to be continuous in all space. A drift is generated due to changes in the magnetic field intensity along the particle orbit.

First we need to consider the magnetic field varying with the position vector in reference to the gyrocenter direction, $r_L(t)$. The motion of the particle is in the direction of the magnetic field, and the position and velocity vector can be decomposed in the gyrocenter direction, and around the field line, such as

$$B(x(t)) = B(x(t)) + r_L(t)) = B(x(t)) + (r_L(t)) \cdot \nabla)B. \tag{3.6}$$

By Taylor expanding the Lorentz equations, and considering the cyclotron motion, we can derive the gyrocenter velocity in the perpendicular and parallel directions as

$$v_{gc}(t) = \left\{ \begin{array}{c} v_{\perp gc}(t) \\ v_{\parallel gc}(t)B \end{array} \right\}. \tag{3.7}$$

Considering that $v_{\perp gc}(t)$ has a slow time dependence, we can approximate the perpendicular gyrocentric velocity as

$$v_{\perp gc}(t) \simeq v_F \equiv \frac{F_\perp \times B}{qB^2}. \tag{3.8}$$

Considering the drift generated by the curvature of the magnetic field, one should just express how the perpendicular force is described in 3.8. Making a gyro average of the perpendicular force in cylindrical coordinates, we get

$$\langle F_\perp \rangle = -2|m|(\frac{1}{2\pi} \oint \frac{\partial B}{\partial r} r d\theta) = -|m|(\nabla B)_\perp. \tag{3.9}$$

The so-called grad B drift becomes

$$v_{\nabla B} = -\frac{|m|}{q}\frac{(\nabla B)\times B}{B^2}. \tag{3.10}$$

Equation 3.10 has a dependence in the particle charge, which means that electrons and ions drift in opposite directions and generate a net electric current. This drift is of great importance for our work, since fast ions have an impact on ∇B, directly affecting the drift of particles.

An effect of fast ions on the α_{MHD} parameter must be pointed out here, since it has an impact in the plasma geometry. α_{MHD} is a magnetohydrodynamic parameter defined as

$$\alpha = -\frac{q^2\beta R\nabla P}{P}, \tag{3.11}$$

where R is the major radius, P the plasma pressure, q the safety factor, and β the ratio between the plasma kinetic and magnetic pressure. The safety factor measures the ratio of the number of times a particular magnetic field line travels toroidally and poloidally. Because the fast ions generate high values of localized pressure, they can affect α_{MHD} in a way that it modifies the plasma geometry, represented by the ∇B on equation 3.10.

High values of α_{MHD} reduce the curvature of the plasma, and instabilities associated with the ∇B, are reduced as well. This effect is associated with the formation of the Internal Transport Barrier (ITB) [17]. The increase of α_{MHD} reduces curvature-type microinstabilities, which augment even more the pressure, amplifying the value of α_{MHD}. This positive feedback is desired because it increases the confinement performance and therefore the total power yield.

3.3 Kinetic theory

In the study of gases, the kinetic theory is responsible for analyzing the particle behavior through a statistical point of view. Macroscopic effects may be extracted from microscopic phenomena. We assume that the particles are smaller than the whole system, and that they follow Newton's law of motion and undergo specific collision processes.

The kinetic theory brings the microscopic effects of particles to a macroscopic analysis through the use of statistical tools. The averaging out of microscopic effects leads to statis-

tic kinetic effects, and these may lead to a further particle-fluid characterization of the plasma.

3.4 Transport theory

From the Boltzmann equation

$$\frac{\partial f(r,v,t)}{\partial t} + v \cdot \nabla f(r,v,t) + a \cdot \nabla_v f(r,v,t) = \left(\frac{\delta f(r,v,t)}{\delta t} \right)_{coll}, \tag{3.12}$$

one can derive a set of equations that describe how transport occurs in magnetized plasma. The plasma macroscopic transport equations are extracted directly from the Boltzmann equation in form of moments of the distribution function. As a result we have a set of equations known as moments of the Boltzmann equations. This moments can be associated with conservation equations of mass, momentum, and energy.

The transport theory is responsible for the study of transfer of quantities between and within a set of systems or a given system. Mass, momentum, and energy are quantities frequently analyzed as macroscopic variables of interest in order to describe plasma dynamics.

3.4.1 Moments of Boltzmann equation

The moments of the Boltzmann equation arise as an attempt to extract macroscopic properties of the system by means of the distribution function and the Boltzmann equation. A way to do so is to take the average of the distribution function in the Boltzmann equation considering the phase space of the independent parameter of the physical variable in consideration. Suppose that a given physical quantity, $\zeta(v)$, is proposed to be studied by the method of moments. First, one should average it out by multiplying it by the Boltzmann equation and integrating it in all space of velocities, then dividing the result by the particle number density.

One is able to retrieve the general transport equation,

$$\frac{\partial}{\partial t}(n\langle\zeta(v)\rangle) + \nabla \cdot (n\langle\zeta(v)\rangle) - n\langle a \cdot \nabla_v \zeta\rangle = \left(\frac{\delta}{\delta t}(n\langle\zeta(v)\rangle) \right)_{coll}. \tag{3.13}$$

The right-hand side represents the rate in which collision modifies the quantity ζ. The parameter ζ could be replaced by the mass or the momentum.

It is important to stress that in the case of this thesis, collisions between fast particles and other plasma species could lead to changes in the transport properties due to a modification in the collision operator. This modification is included in the right hand side of equation 3.13, and the impact on the transport is represented by the conserved quantities derived in section 3.4.2.

3.4.2 Conserved quantities

From the principle of taking moments of the Boltzmann equation described in Appendix A, one may derive important relations that are helpful to understand how transport takes place in the plasma. A complete derivation is also found in appendix A.

The following equation is known as the continuity equation. The term ρ represents the mass density $n \cdot m$, and $\mathbf{u}$ is the linear velocity. Here, S represents the collision term

$$\frac{\partial \rho_m}{\partial t} + \nabla \cdot (\rho_m \mathbf{u}) = S. \tag{3.14}$$

By considering a collisionless scenario, dividing A.4 by the mass m, and multiplying the whole equation by the charge of the species, one may arrive at the conservation of the electric charge equation

$$\frac{\partial \rho_q}{\partial t} + \nabla \cdot \mathbf{J} = 0, \tag{3.15}$$

where $\rho_q = n \cdot q$ is the charge density and $\mathbf{J} = \rho_q \mathbf{u}$ is the current density.

Those equations are important because they show that the mass and electric charge are conserved properties in the plasma transport dynamics. The charge and mass balance must be correct when fusion reactions take place and mass is transformed into energy.

Another important conservation is the momentum conservation

$$n\, m\, \frac{Du}{Dt} = n\, q\, (E + u \times B) - \nabla \cdot \overleftrightarrow{\Psi} - \delta, \tag{3.16}$$

where $\overleftrightarrow{\Psi}$ is the dyadic of pressure generated by the friction arising from the random movements w_i and w_j of the particles in different layers of the plasma. It represents how the rate in change of momentum varies with the collision term δ, the internal pressure in the plasma and the Lorentz force. That is another important restriction in the transport theory,

since the collision between particles cannot create more momentum after the event happened.

The energy conservation is expressed as

$$\frac{N}{2}\frac{D\overleftrightarrow{\Psi}}{Dt}+\frac{2+N}{2}\overleftrightarrow{\Psi}\nabla\cdot u=-\nabla\cdot Q+\delta\cdot u-(\frac{\partial W}{\partial t})_{coll}. \tag{3.17}$$

Here $\delta\cdot u$ represents the heating due to friction processes, and $(\frac{\partial W}{\partial t})_{coll}$ the energy transferred by collisions.

3.5 Neoclassical transport

Until now, we have reviewed the classic theory and how the fast ions affect the plasma geometry and transport in this framework, i. e. through the geometry in α_{MHD} and the ∇B, and through the collision operator in 3.13. Some further considerations must be done in order to accurately describe the transport of particles and heat in tokamak devices. In this section we further analyze the construction of the collision operators and the geometry description of the phenomena.

3.5.1 Random walk approach

A random walk consists of a movement that in principle has no determined pattern, and it is random by definition [18]. It is expressed as a succession of random steps. By using this argument, we are capable of deducing some transport coefficients perpendicular to the magnetic field B.

Considering the collision of particles in their gyromotion orbits as a random process, the diffusion coefficient is described as $D\sim\frac{\langle(\Delta x)^2\rangle}{\Delta t}\sim\rho^2\nu$, as seen in the Appendix B. Here Δx is the mean free path and Δt is the time between collisions. Any step with size comparable to ρ, the Larmor radius, is considered classical transport. Diffusivity terms are also related to the gradient of temperature through $S=D\cdot\nabla T$, where T is the temperature and S is the source. In the case that fast ions are driven through ICRH, the change in the gradient of temperature is proportional do the diffusivity D.

In order to correct the conservation equations, consider a small parameter ε related to the collisional time and macroscopic time scale and a Maxwellian distribution function,

assuming $T_e = T_i$ and $V_e = V_i$.

The zeroth order of the conservation equations originated from the above approach can be seen when the Fokker-Planck collision operator for conserved particles is considered. We have for the density

$$\frac{\partial n_s}{\partial t} + \nabla \cdot (n_s u_s) = 0, \tag{3.18}$$

where $n_s = \int f_s d^3v$ and $u_s = \frac{1}{n_s}\int f_s v d^3v$, are the density and averaged velocity. For the momentum conservation, one would get

$$m_s n_s \frac{Du_s}{Dt} = Z_i e n_s (E + u_s \times B) - \nabla p_s - \nabla \cdot \Pi_s + R_{s,s'}. \tag{3.19}$$

In the right hand side, we find terms corresponding to the Lorentz force, pressure, viscous force and frictional forces, respectively. The same path could be followed in order to demonstrate the respective equations for energy and heat flux conservation. It is interesting to point out that, for the case of flux conservation, a parallel, crossed (diamagnetic), and perpendicular components are described. For the ions we have

$$q_i = -k_{\|i} b(b \cdot \nabla) T_i + k_{\Lambda i} b \times \nabla T_i - k_{\perp i} \nabla_\perp T_i. \tag{3.20}$$

The relations for $k's$ are $k_{\|s} \sim n_s \nu_s \lambda_s^2$, $k_{\Lambda s} \sim \frac{\nu_s}{\omega_s} k_{\|s}$, and $k_{\perp s} \sim n_s \nu_s \rho_s^2$.

These equations are still limited if compared to real cases. The parallel and perpendicular gradient scale lengths of macroscopic quantities must be large in comparison to the collision mean free path and gyroradius, respectively. Macroscopic quantities have, also, a moderated rate of change when compared to collision frequency. Small scale processes may appear, but they are averaged out from the net transport, they would have to be described by kinetic characterization and then added to the above equations.

In Appendix C, a precise derivation of the flux is made. The resulting relation is

$$\Gamma_\Psi^{neo} = -\frac{I}{q}\left\langle \frac{1}{B^2}\left[nq(B\cdot\nabla)\phi_1 + (B\cdot\nabla)p_1 + B\cdot\nabla\cdot\Pi\right]\right\rangle \tag{3.21}$$

$$= nI\left\langle \left(\frac{1}{B^2} - \frac{1}{\langle B^2\rangle}\right)\left(\frac{J_\| B}{\sigma_\|} - E_\|^A B\right)\right\rangle + \frac{nI}{\langle B^2\rangle}\left\langle \frac{J_\| B}{\sigma_\|} - E_\|^A B\right\rangle. \tag{3.22}$$

The first bracket represents the Pfirsch-Schlüter transport, a transport that happens within the flux surface, due to friction parallel to the background magnetic field, and the second one, averaged over the flux surface, is the Banana-Plateau, associated to particles with trapped orbits. If a radial density gradient is considered, on the low field side (region where magnetic field is less intense) more co-trapped particles than counter-trapped are found, which means that a co-current density is formed. The banana current flows in the co-direction, in order to break the anisotropy in the velocity distribution.

The total current within the flux surface, considering the charge continuity equation, is

$$J_{\|}B = -I\frac{d}{d\Psi}(p_e + p_i)(1 - \frac{B^2}{\langle B^2\rangle}) + \frac{\langle J_{\|}B\rangle B^2}{\langle B^2\rangle}. \tag{3.23}$$

The first term in the right hand side is the Pfirsch-Schlüter current, resulting in a diffusive flux $\Gamma^{PF} \sim q^2(\Psi)D_{classic}$ and larger than the classical diffusion values.

Further considerations must be made in order to close the neoclassical transport description. A generalization of the Braginskii equations for any ratio of mean free path to gradient lengths must be done as well as losses processes in the case of open field lines and better accounting for effects of viscosity must be also taken into consideration.

3.5.2 Neoclassical transport

Perpendicular diffusion can be estimated with the random walk argument and is directly related to the Banana regime, where $D \sim \nu\rho^2 q^2/\varepsilon^{3/2}$. Depending on the collision frequency, the banana orbit may be completed or not, arriving to the point of drift off from the flux surface, where $D \sim w_b\rho^2 q^2/\varepsilon^{3/2}$, and w_b is the untrapped particle bounce frequency. In the highest collision frequency cases, Pfirsch-Schlüter Diffusion dominates with $D \sim \nu\rho^2 q^2/\varepsilon^{3/2}$, and $\nu >> w_b$.

A more detailed neoclassic description is possible when ion perpendicular heat transport takes an important role, and it dominantly affects the whole transport. Perpendicular transport is highly scaled with collisionality, going from banana to Pfirsch-Schlüter regime depending on the frequency ν as seen in figure 3.1. Electrical conductivity is decreased due to trapped particle effects and the Bootstrap current, the parallel component of viscous damping of poloidal electron diamagnetic flow and an important neoclassical prediction. Effects on viscous damping of poloidal flows, where passing particles carry flow and collide with

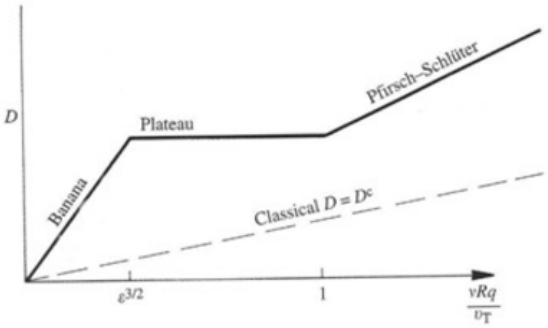

Fig. 3.1 Diffusivity as function of collisionality regime.

stationary trapped particles, are also taken into account.

Bootstrap current is driven by density and temperature gradient. It is independent of other current drive mechanisms and provide most of the poloidal field in advanced tokamak scenarios.

By applying the Braginskii approach in the framework of the neoclassical transport, and generalizing the parallel viscous stress, we can modify the viscosity, Π, in order to have a better description of the banana-plateau regime .

The total neoclassical transport is obtained by putting together Classical, Banana-Plateau, and Pfirsch-Schlüter transports is

$$\Gamma = \langle nV \cdot \nabla\Psi \rangle = \left\langle \frac{1}{B^2} \nabla\Psi \cdot B \times \left(\frac{nqJ_\perp}{\sigma_\perp} + nq\nabla\phi_1 + \nabla p_1 + \nabla \cdot \Pi_{\|} \right) \right\rangle . \tag{3.24}$$

Here, the first term inside the right hand side parenthesis accounts for the classical transport, and the last three terms for Pfirsch-Schlüter and Banana-Plateau transport. A more detailed derivation is made in Appendix C.

The present model is still not capable of predicting real values of experimental heat and particle flux, believed to be mostly driven by turbulence and micro-instabilities [19]. Perpendicular Ion heat transport in large tokamaks is responsible for more heat flux than theoretically predicted. The amount of transport that exceed the neoclassical levels are called Anomalous Transport. In the present work, we assume that this issue is resolved with the support of the gyrokinetic turbulent theory.

3.6 Turbulence and the Gyrokinetic theory

3.6.1 Bohm diffusivity

After it was observed that the neoclassical predictions and experiments differ by orders of magnitude [19], the study of a new transport mechanism led to the establishment of the Bohm diffusion, as determined by anomalous processes. The Bohm diffusion coefficient is characterized by the following proportionality

$$D^{(B)} \simeq \frac{K_B T}{eB}. \tag{3.25}$$

Here, the diffusion is directly related to the magnetic field strength B, the Boltzmann constant K_B and the temperature T. It is important to keep in mind that the level of transport is determined empirically. It matched better the experimental results and gave insights in the directions that a turbulent theory must follow in terms of diffusivity.

3.6.2 Turbulent mechanism

Turbulence is thought to be the mechanism in which fluids dissipate energy input from large scales to small scales, releasing it in the form of heat. The apparent random behavior of turbulent flows does not necessarily means that it is not deterministic, and therefore, a mathematical approach can be developed in order to comprehend the mechanism.

In magnetically confined plasmas, the role of turbulence is also understood as a means to energy dissipation from larger to small scales. The turbulent regime is characterized by small fluctuations in the mean plasma parameters, such as pressure, electric field and temperature. In this case, the energy is passed from larger scales to small ones, through cascades, where the energy can be finally released in the form of heat, as schematized in figure 3.2.

In order to describe turbulent behavior, we are going to work in the framework of the Gyrokinetic description. The fluctuations present in the parameters of interest can be analyzed in more detail.

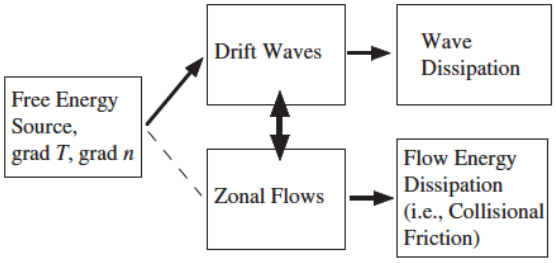

Fig. 3.2 Dissipation pathways within turbulent framework [4].

3.6.3 Gyrokinetic approach

The gyrokinetic approach to the study of plasma dynamics allows to describe perpendicular waves with $k_\perp \simeq \rho_{e,i}$, where $k_\perp$ is the typical wave number perpendicular to B, and $\rho_{e,i}$ is the gyroradius, and with time scales smaller than the ion cyclotron frequency. In order to compute the parameters of interest, one needs first to compute the distribution function.

From the Fokker-Planck equation, one must rewrite the main parameters in terms of a perturbed expansion. The expanded equation is described as [20]

$$\left[\frac{\partial}{\partial t} + v\cdot\nabla + \frac{q}{m}\left(v\times(B+B_p)+(E+E_p)\right)\cdot\frac{\partial}{\partial v}\right](f+f_p) = C[f+f_p]. \tag{3.26}$$

In order to isolate the perturbed part, indicated with an sub index "P", one could subtract from the previous equation its average, leading to

$$\left[\frac{\partial}{\partial t} + v\cdot\nabla + \frac{q}{m}\left(v\times B+E\right)\cdot\frac{\partial}{\partial v}\right] f_p = \frac{q}{m}\left(v\times B_p + E_p\right)\cdot\frac{\partial(f+f_p)}{\partial v} - \Xi + C - \langle C\rangle_{average}\,. \tag{3.27}$$

Here, it is important to notice that there is a crossed effect of the main value of the distribution function on the perturbed part of the main parameters, represented on the right hand side of the equation. The last term on the right hand side is an operator responsible for the description of the averaged out interaction between the fluctuations with the particles of the system $\Xi = -\frac{q}{m}\left\langle (v\times B_p + E_p)\cdot\frac{\partial f_p}{\partial v}\right\rangle_{average}$. Passing the frame of reference to the one coinciding with the guiding center of the particle's orbit, the dimensionality and complexity of the problem is reduced. Since the cycloid behavior of the particle around its guiding center is reduced to the movement of a parallel velocity, $v_{||}$, a magnetic moment described as

$$\mu = \frac{m v_{\perp}{}^2}{2B}. \tag{3.28}$$

A first order guessed solution of equation 3.27 is described as the adiabatic and non adiabatic solution of the perturbed distribution

$$f_{p,1}(r) = -\frac{q\phi_p(r)}{T} + H(r), \tag{3.29}$$

in terms of the gyrocenter position r. Considering

$$h(r) = H(r) - \frac{q f_{p,0} \Im(r)}{T}, \tag{3.30}$$

and

$$\Im_p(r) = \left\langle \phi_p(r) - v \cdot A_p(r) \right\rangle_{average}. \tag{3.31}$$

The next order solution of the gyro-averaged equation is described as

$$\frac{\partial h}{\partial t} + (\hat{n} v_{\parallel} + v_d) \cdot \nabla H + v_p^d \cdot \nabla h - C[H] = -v_p^d \cdot \nabla f_0. \tag{3.32}$$

Here the perturbed drift velocity is

$$v_p^d = \hat{n} \times \nabla \Im_p / B. \tag{3.33}$$

Even when considered as a linear approach to the gyrokinetic theory, equation 3.32 has a complex solution, which makes it hard to be analytically solved regardless of the simplicity of the chosen geometry. High performance computing simulations are the most suitable answer for the solutions of such problems.

3.6.4 Ballooning properties

It is interesting to notice that, turbulence in plasma is normally elongated in the direction of the magnetic field, in the torus around the plasma bulk. Despite of that, a small perpendicular component exists. A way to study these small perpendicular perturbations is to represent them in a flute-like description proportional to $e^{i(m\chi - n\phi)}$, where m, and n are integer numbers, and χ is the poloidal, and ϕ is the toroidal coordinates.

Since the microinstabilities modes are not localized, but in fact spread over different flux surfaces, one could use, instead of a flux approach, a ballooning representation, and compact the small perpendicular and elongated parallel modes. Disregarding the time dependence, and

using a toroidal harmonic description of the perturbed fields X_p, we can have the expression in a compact form as [21]

$$X_p(r,\chi,\phi) = x_{p,n}(r,\chi)e^{-in[\phi-q(r)]\chi}. \tag{3.34}$$

Considering a ballooning function depending on the poloidal angle χ.

Observe that simple modes are radially periodic, and in order to simplify the approach, the constant parameters over the radial domain could be approximated leading to a flattened profile. This is useful when $\rho \to 0$, and the perturbed parameters can be expanded in a perpendicular direction.

One can describe the non adiabatic part of the distribution h in a ballooning representation as [22],

$$\frac{v_\parallel}{qR}\partial_\theta h - i(w-w_D)h - C[h] = -i\frac{qf_0}{T}(w-w_T')\phi J_0(z), \tag{3.35}$$

where h, and ϕ are perturbed functions of the Ballooning description. Since the time derivatives are in function of the frequency, w_T is proportional to w', the diamagnetic frequency, q is the safety factor, C is the collision operator, and w_D is the magnetic drift frequency.

3.6.5 Fluxes

To understand how turbulence arises in the gyrokinetic theory, we analyze the potential perturbation ϕ_p, corresponding to a perturbed drift velocity described in 3.33

$$v_p^d = \frac{\hat{n}\times\nabla\phi_p}{B}, \tag{3.36}$$

generating ambipolar effects. The average over a flux surface of this flow gives the particle flux. Its dependence on the perturbed density n_p, and its relation to the perturbed potential are one of the indicators of its perturbed property.

Considering that $(\hat{n}\times\nabla\phi_p)\cdot r = ik_\theta\phi_p$, being r the unit vector in the radial direction, one can define the particle flux as

$$\Gamma = -\left\langle \frac{k_\theta T n}{qB}\left|\frac{q\phi_p}{T}\right|^2 \Re\left[\frac{n_p/n}{q\phi_p/T}\right]\right\rangle. \tag{3.37}$$

Here the operator $\Re$ represents the density response of the plasma, and the right hand side is averaged in a flux surface. For a heat flux, a similar operator is responsible for represent the plasma temperature response

$$Q = -\left\langle \frac{k_\theta T^2 n}{qB} \left| \frac{q\phi_p}{T} \right|^2 \Re \left[\frac{T_p/T}{q\phi_p/T} \right] \right\rangle, \tag{3.38}$$

also averaged out over a flux surface. Notice that the perturbed properties of these quantities depend on the fact that the density, or temperature, perturbations are not aligned with the perturbed potential. If one thinks about the non adiabatic electron response, the particle flux is non existent if one does not consider impurities, and in this approximation the adiabatic part of f_p does not lead to any flux in the radial direction.

As we will to see in chapter 4, where the simulation codes are introduced, the gyrokinetic code GENE [23] computes the flux in an analogous way. Accurate solutions of those fluxes require enormous computational resources, hence the need of codes such as GENE running in High Performance Computing environments.

GENE computes the heat flux, and due to the behavior of particles and heat between flux surfaces, it computes also the zonal flow. The zonal flow is the flow of plasma within a flux surface in the poloidal direction. It is localized in their radial extent transverse to the magnetic surfaces and it is a self-organized phenomenon driven by drift-type modes.

Gyrokinetic codes follow the evolution of the distribution functions of all species, each of them contributing to the collective fluctuations of the electrostatic potential and the magnetic field. Fast particles can influence the turbulence that is carried by thermal particles. If no intrinsically fast particle driven fluctuations are excited, this interaction can result in turbulence reduction.

Chapter 4

Simulation codes

In order to study the impact of fast ions on microturbulence stabilization, and to explain the peak of ion temperature in the experiments described in chapter 2, we make use of two main codes. FIDO [24] simulates the power deposition from the antenna's waves into the plasma, and it uses the electromagnetic wave parameters from PION [25]. GENE [23] simulates plasma fluctuations and therefore the transport coefficients. In the present chapter, a brief discussion of these codes is presented.

4.1 GENE

The GENE, acronym for Gyrokinetic Electromagnetic Numerical Experiment [23], is an open source plasma microturbulence code which can be used to efficiently compute gyroradius-scale fluctuations and the resulting transport coefficients in magnetized fusion and astrophysical plasmas. To this aim, it solves the nonlinear gyrokinetic equations on a fixed grid in five-dimensional phase space, and time. The code can be solved in a flux-tube mode, radially global or flux-surface global configuration. In the present work, only flux-tube simulations are considered. Neoclassical transport equations are included in it. The GENE code is highly parallelized, and it runs on various of the world's powerful supercomputers architectures.

As we have seen in section 3.6.3, fast gyromotion can be analytically removed from the Boltzmann equation, which allows to neglect the fast gyromotion and choose a larger timestep for numerical simulations. In GENE, the computed quantities are the time-dependent distribution function of electrons, the main ion, and other particle species in a five-dimensional phase space. It also computes the Maxwell field equations. Remembering that now, due to the gyrokinetic approach, the helical movement around the field lines is reduced to a linear

movement of a magnetic dipole.

It is considered that in the flux-tube approximation, as seen in the left hand side of image 4.1, the neoclassical equilibrium contained in the gyrokinetic equations decouples as a non-fluctuating part, and then both parts can be solved separately. The code considers magnetic fluctuations perpendicular and parallel to the background field. Collisions between all species are computed with a Landau-Boltzmann operator, which is discretized with a finite volume scheme. For considering general magnetic configurations, GENE features interfaces to various equilibrium codes, but also analytical models, such as "Miller" and "s-alpha" can be used.

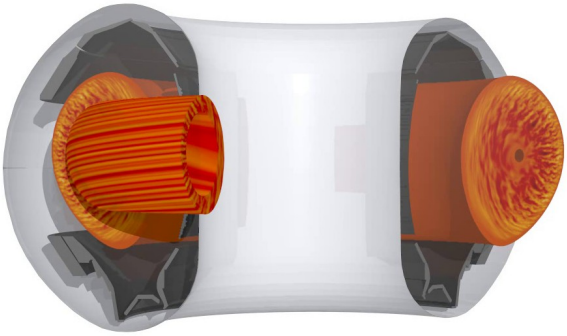

Fig. 4.1 Global GENE simulation of AUG reactor. Figure courtesy of genecode.org

The five phase space dimensions are discretized using various techniques. Spectral methods are applied in x and y, i. e. the two coordinates perpendicular to the magnetic field, where fast Fourier transforms are required for computing the ExB nonlinearity in direct space. Derivatives in the parallel coordinate z and the parallel velocity $v_{\|}$ use a two-dimensional Arakawa discretization, while integrals are performed with a trapezoidal rule. Integrals in μ are performed by a Gauss-Laguerre quadrature.

In order to solve the eigenvalue spectrum of the linear gyrokinetic operators, GENE uses the SLEPc, which builds on the PETSc linear algebra package [26]. GENE can be simulated in a linear and nonlinear mode. In the linear mode, the instability growth associated with one instable mode is simulated, presented by K_y in the code. Meanwhile, in the nonlinear mode, all instable modes are simulated, which means all K_y are computed. The flux levels are only simulated in the nonlinear mode. In order to solve the eigenvalue problems, it repeatedly applies matrix-vector multiplications representing the evaluation of the linearized gyrokinetic equation. In a non HPC (High Performance Computing) environment, solving the nonlinear time evolution of such equations would take up to a decade in one CPU. On HPC systems

such as the ones used in the present work, a typical nonlinear simulation takes around 48 hours to finish.

Besides eigenvalues computations, GENE can also be run as an initial value solver. Starting from an appropriate initial condition, the distribution function f is advanced with the Vlasov equation using explicit fourth-order Runge-Kutta time-stepping. To determine the maximum stable time-step, the eigenvalues of largest magnitude are computed with SLEPc. Depending on the number of grid points, eigenvalue computations or initial value runs can be faster. Nonlinear simulations can only be performed as an initial value problem.

For nonlinear simulations, the capability to run in many processors at the same time is essential in order to have the results of the simulation within a life-time period. A typical non-linear GENE simulation has a n_{x0} box size dimension equal to 256, and L_x equal to $128\rho_s$, with ρ_s equals the Larmor radius over minor radius. For the phase space we have $256 \times 128 \times 24 \times 32 \times 12 \times 2$ grid points for the main parameters (x, y, z, $v_{\|}$, μ and species), totalizing 603.979.776 grid points.

GENE is parallelized on supercomputing architectures using the domain decomposition technique. In this sense, larger arrays are distributed among available processors. For derivatives and integrals, information from other processors is required, which is exchanged by the message passing interface (MPI). Shared memory approaches like OpenMP and GPUs are explored, but not in routine use.

4.1.1 The equations

An equation of interest solved in the GENE code is the Gyrokinetic Vlasov equation for the different species. Taking in consideration the collision operator, as well as advective and diffusive terms in the velocity space, we have

$$\frac{\partial f}{\partial t} + \dot{X} \cdot \nabla f + \dot{v}_{\|} \frac{\partial f}{\partial v_{\|}} + \dot{\mu} \frac{\partial f}{\partial \mu} = C(f), \tag{4.1}$$

where f represents the distribution function of a given species. It must be taken in consideration that $\dot{\mu} = 0$, and that the term $\dot{X}$ represents the gyrocenter position and is described as

$$\dot{X} = v_{\parallel}\hat{n}_0 + \frac{B_0}{B_{0,\parallel}}v_{\perp}. \tag{4.2}$$

This approach optimizes the computation of microturbulent fluctuations, while the approach used in chapter 3 is more general and descriptive, constructed to outline the different interplays in plasma transport.

The drift velocities must also be taken care of. GENE combines them in one single equation, creating a dependence with a generalized potential

$$v_{\perp} \equiv \frac{c}{B_0^2}\chi \times B_0 + \frac{\mu}{m\Omega}\hat{n}_0 \times \nabla B_0 + \frac{v_{\parallel}^2}{\Omega}(\nabla \times \hat{n})_{\perp}. \tag{4.3}$$

The Curvature and ∇B drift can be combined into the magnetic drift, where by a pressure gradient term is consistently taken into account. Together with considering $B_{\parallel}$ fluctuations, this provides the most accurate description of electromagnetic effects in the local gyrokinetic framework.

Consider the generalized potential as

$$\chi = \overline{\phi}_1 - \frac{v_{\parallel}}{c}\overline{A}_1 + \frac{\mu}{q}\overline{B}_{1,\parallel}, \tag{4.4}$$

where the bar denotes the gyroaverage. Considering the electric field described as

$$E_1 = -\nabla\phi_1 - \frac{\hat{n}_0}{c}\frac{\partial}{\partial t}A_{1,\parallel}. \tag{4.5}$$

The parallel velocity is computed as

$$\dot{v}_{\parallel} = \frac{\dot{X}}{mv_{\parallel}} \cdot (q\overline{E}_1 - \mu\nabla(B_0 + \bar{B}_{1,\parallel})). \tag{4.6}$$

In equation 4.6, it is important to notice the dipole momentum connection with both the initial and parallel perturbed magnetic fields.

In order to solve the problem, Ampere's law and the Poisson equation needs to be implemented in the gyrokinetic framework

$$\nabla_{\perp}^2\phi_1 = -4\pi\sum qn_1. \tag{4.7}$$

In which n_1 is related to the density perturbation, and

$$\nabla_{\perp}^{2} A_{1,\parallel} = -\frac{4\pi}{c} \sum j_{1,\parallel}, \tag{4.8}$$

$$B_{1,\parallel} = -4\pi \sum \frac{p_{1,\perp}}{B_0}. \tag{4.9}$$

Here the current perturbation, j_1, is summed over all the species.

In a local approximation, the moments can be described in a Fourier space as

$$n_{1,k} = \frac{2\pi B_0}{m} \int dv_{\parallel} d\mu \left[J_0 h_{1,k} - q\phi_{1,k} \frac{F_0}{T_0} \right], \tag{4.10}$$

$$j_{1,\parallel,k} = q \frac{2\pi B_0}{m} \int dv_{\parallel} d\mu v_{\parallel} \left[J_0 h_{1,k} - q\phi_{1,k} \frac{F_0}{T_0} \right], \tag{4.11}$$

and

$$p_{1,\perp,k} \equiv \frac{2\pi B_0}{m} \int dv_{\parallel} d\mu \mu B_0 I_1 h_{1,k}. \tag{4.12}$$

Considering the non adiabatic part of f_1 as

$$h_1 \equiv f_1 + \left[qJ_0\phi_1 + \mu I_1 B_{1\parallel} \right] \frac{F_0}{T_0}. \tag{4.13}$$

It is necessary to recall that h_1 must be computed for each one of the species considered in the problem. The Bessel function J_0 is given by

$$J_0 = J_0(k_{\perp}\rho), \tag{4.14}$$

and we have introduced

$$I_1 = I_1(k_{\perp}\rho) = 2\frac{J_1(k_{\perp}\rho)}{k_{\perp}\rho}. \tag{4.15}$$

4.1.2 Outputs

After the simulation is finished, GENE has a large number of output files written in the desired directory. The main output are time trace information such as density and three-dimensional information about the fields and moments of the distribution function.

The normalized fluctuating quantities are spatially averaged with respect to the full simulation volume. Considering $f^{pc} = h_1 - q_\phi \frac{F_0}{T_0}$ the particle distribution function, the heat and parallel momentum fluxes are computed as

$$\Gamma = \int d^3v f_1^{pc} v_D, \tag{4.16}$$

$$Q = \int d^3v (\frac{1}{2} m v^2) f_1^{pc} v_D, \tag{4.17}$$

and

$$\Pi = \int d^3v (m v_\parallel) f_1^{pc} v_D. \tag{4.18}$$

Where v_D is the generalized $E \times B$ velocity drift. The fluxes are divided into an electromagnetic and electrostatic radially projected components.

The field quantities are given as a function of time in three dimensions (k_x, k_y, z)

$$\phi_1 \left\{ A_{1\parallel} \left[B_{1\parallel} \right] \right\}. \tag{4.19}$$

In this case $A_{1\parallel}$ and $B_{1\parallel}$ are only computed in the electromagnetic case.

For each of the computed species, the velocity space moments are given. Their average combination yield the parallel heat current density

$$q_{1\parallel} + 1.5 p_0 u_{1\parallel} = \frac{1}{2} \int d^3v v_\parallel^3 f^{pc}, \tag{4.20}$$

$$q_{1\perp} + p_0 u_{1\parallel} = \frac{1}{2} \int d^3v v_\parallel v_\perp^2 f^{pc}. \tag{4.21}$$

Here $u_{1\parallel}$ is defined as

$$u_{1\parallel} = \frac{1}{n_0} \int d^3v v_\parallel f_1^{pc}. \tag{4.22}$$

Further outputs on GENE include neoclassical results, information about the velocity space, information about instabilities growth rates γ and frequencies ω, apart of the checkpoint files.

4.2 FIDO

The Monte Carlo Finite Ion Drift Orbit code computes the time evolution of the distribution function of resonating ions during ICRF heating in tokamak reactors [24]. Because of the non-Maxwellian high-energy tail developed by the ion species during such process, a detailed study of their behavior must be made. FIDO separates the different orbits for the heated species in a 2D plane, enabling the detailed study of the contribution of each of those orbits.

FIDO calculates fast ion pressure, density and temperature profiles. These profiles are used as input in GENE in order to represent the ICRF-heated species. The code assumes a finite width of the orbits, and different profiles of power absorption are computed. It also includes an RF-induced spatial diffusion due to toroidal momentum generated by the waves. Such considerations have an impact on the computation of the density profile of the resonating ion species.

4.2.1 Theoretical formalism

To describe the evolution of the fast ion distribution function, FIDO solves the Fokker-Planck equation in the presence of Coulomb collisions and considering also a second operator known as wave-particle interaction operator

$$\frac{\partial f}{\partial t} + \dot{z} \cdot \frac{\partial f}{\partial z} = C_f + Q_f. \tag{4.23}$$

In equation 4.23, f represents the distribution function of the resonant species in q phase-space coordinate, C is the Coulomb collision operator and Q is the operator that describes the interaction between particles and the electromagnetic wave.

In the Monte Carlo form, the collision between particles and the wave-particle interaction cause diffusion of the particles in the phase-space. Together with the drift effects, taken into account through Monte Carlo increments, FIDO describes the deterministic and the stochastic motion through uncorrelated random numbers. In a tokamak, the undisturbed motion of the particles is integrable, which means that the constants of motion have the same dimensionality of the degrees of freedom of the system. In FIDO, the Hamiltonian of the system is put in the form of three action variables, which are the constants of motion of the system.

Chapter 5

Microturbulence stabilization

In the present chapter we analyze the results obtained with FIDO and GENE in order to quantify the impact of fast ions on the stabilization of microturbulence in linear and nonlinear modes. We also discuss whether the analysis could be further improved with the addition of newer features implemented in GENE.

Our goal is to quantify the impact of fast ions stabilization using numerical tools. As we have seen in the chapter 3, different mechanisms allow for an active reduction of transport. These mechanisms are implemented in the numerical tools described in chapter 4. We further discuss how this stabilization is possible from the theoretical point of view. This work considers two ASDEX Upgrade discharges, presented in Chapter 2, although most of the analysis focus on discharge 31563, where a higher value of central ion temperature is measured and the stabilizing effect is found to be stronger.

5.1 FIDO analysis

FIDO calculates the distribution function of the fast ion population in tokamaks. In the code, one inputs the electron and main ion density profiles, as well as parameters related to the electromagnetic wave interaction with the plasma such as number of toroidal or the fraction of the coupled power in each mode. In this thesis, the parameters used in FIDO were extracted from the experimental ASDEX Upgrade database. For the electromagnetic wave parameter, the PION code was used.

PION [25] calculates the time-dependent ICRH power deposition profile and the distribution function of resonating ions self-consistently using simplified models. It helps to establish

the proper set up of electromagnetic wave parameters in FIDO, that in turn calculates the resulting fast ion final distribution function, taking into account the finite orbit width effects and RF- induced spatial diffusion.

5.1.1 Results

FIDO gives the power transfered from the fast ions to electrons and to the bulk ions, i. e. the main species. In figure 5.1 we can see the profile of power deposition to the main ions. As expected from the ICRH theory, most of the energy is deposited around the resonance position, with a more steep deposition profile being the one for 31563, where the ICRH gives rise to a more central deposition.

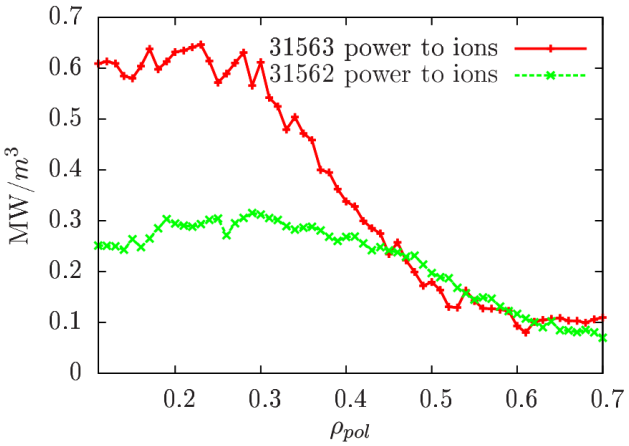

Fig. 5.1 Radial profile of power density transferred from ^{3}He ions to bulk ions.

From FIDO, one can also extract the resonating ion pressure profile. This profile is important because it shows how the fast ions are distributed in radius by ICRH. Figure 5.3 shows the radial profile of the fast ion pressure for discharges 31563 and 31562.

The results obtained for ICRH parameters and radial ^{3}He ICRH absorption profile have been compared to the ones from TORIC and PION, and are in good overall agreement. This comparison gives an extra confidence in the use of FIDO as a tool to generate parameter used in GENE.

The power density to the bulk ions is larger by a factor of 2 in the central plasma region for discharge 31562. This indicates a high value of ICRH deposition close to the on-axis region

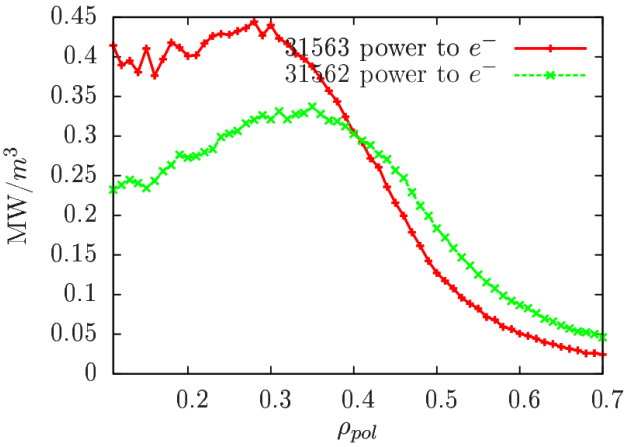

Fig. 5.2 Radial profile of power density transferred from ^{3}He ions to electrons.

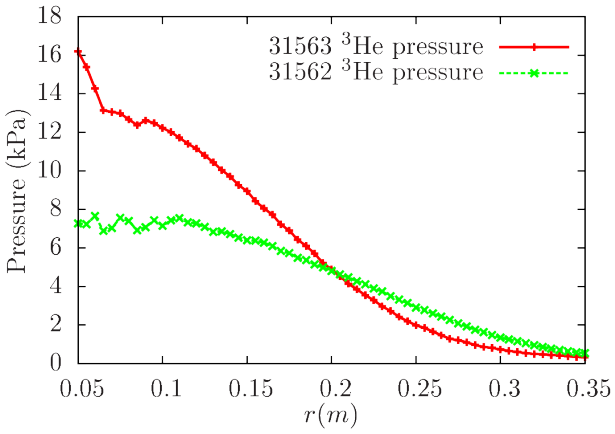

Fig. 5.3 Pressure profile of ^{3}He ions.

of the plasma, although the radial profile of ^{3}He pressure and power density to electrons show a smaller difference in the same plasma region. It is important to keep this behavior in mind, since later we argue on how the stabilizing effect on ITG can be studied separated from the electron dynamics.

In order to compare the transport values and ion temperature stiffness with earlier studies, we estimated $R/LT_i \approx 20$ and the flux is $\approx 1.6 q_i^{gB}$ at $\rho = 0.25$ for discharge 31563. This value of ion heat flux normalized to gyro-Bohm units q_i^{gB} and R/LT_i are typical of H-mode discharges. It is important to stress that R/LT_i is large, and we look for the way in which the presence of fast ions reduce turbulence and allow for such high values.

It is interesting to notice that although the fast ion concentration is low, around 5% at $\rho = 0.25$, the increase in the central ion temperature is almost 80%. It indicates that a strong role is played by the ICRH in the increase of ion bulk temperature through a mechanism in which microturbulence is directly stabilized due to fast ions.

After the FIDO simulations are performed, the fast ion density, temperature and pressure profile were extracted, and the gradient profile is generated. With these quantities, one can generate the fast ion input parameters for GENE, and to study the impact of fast ions with this density, temperature and pressure profiles.

5.2 GENE analysis

To study the stabilization on both discharges, a series of linear scans were performed in GENE. The scan function of GENE was explained in the chapter 4. We first study the impact of electromagnetic effects isolated of fast ion impact. This helps to understand how intense is the electromagnetic effects on the plasma, and further characterize the observed specific behaviors.

To quantify the impact of fast ions on microturbulence, we make use of the pressure profiles generated with FIDO at the position $\rho = 0.25$, corresponding to $r = 0.12$m. In order to simulate the fast ion content on GENE, the following parameters are used as input data.

Fast ion parameters						
discharge	a/L_T	a/L_n	n	T	q	m
31562	1.810	0.670	0.015	23.373	2	1.5
31563	2.532	2.678	0.029	16.978	2	1.5

Here a/L_T stands for the gradient of the temperature, defined as $a/L_T = a/T(dT/dr)$, a/L_n stands for the gradient of the density, defined as $a/L_n = a/n(dn/dr)$, T stands for the temperature and n the density. q and m represents the charge and mass, in terms of the electron charge, and hydrogen mass. All units in GENE are normalized to the reference units.

The tokamak geometry is simulated using the 'miller' function on GENE. It allows to generate a set of parameters extracted from a CLISTE equilibrium [27] reconstruction of the discharge in consideration. This is done with the help of a python subroutine of GENE called 'extract_miller_from_eqdsk'. To account for the high uncertainty in the

safety factor q, we perform scans in this parameter. The pressure gradient in the equilibrium is computed consistently; when fast ions are included, their pressure gradient is accounted for.

In order to study ITG microturbulence stabilisation, it is required to work in a regime that is stable to kinetic ballooning modes (KBM). Otherwise, high transport values are obtained. A series of spectral analyses is performed in order to study the impact of the safety factor q on KBM modes. It is found that KBM is sensitive to q and becomes stable below q=1.5.

After the linear simulations are performed, a set of parameters are chosen to be simulated in nonlinear mode. The statistic average of the heat flux time traces are compared to the experimental values.

5.2.1 Linear results

Results from the linear simulations are displayed in the figures below. Figure 5.4 and 5.5 show the scaling of the instability growth rate with the safety factor.

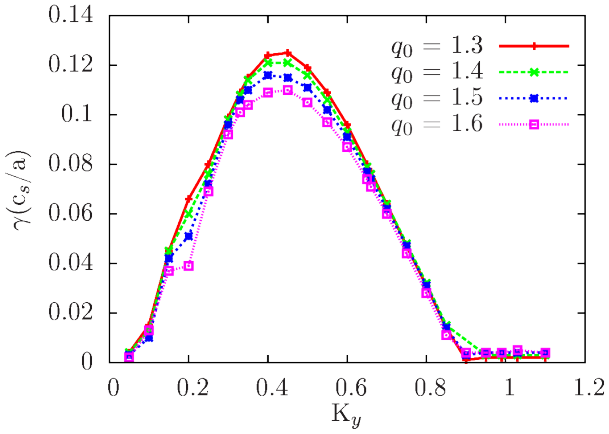

Fig. 5.4 Spectral analysis and safety factor sensitivity scan for discharge 31562.

The scaling with q seen in spectral analysis from figures 5.4 and 5.5 show that both discharge have high electromagnetic activity. In the electrostatic limit, one would obtain the opposite trend [28], in which high values of safety factor q yield higher growth rates. High electromagnetic activity is also detected in figures 5.6 and 5.7. Here we also can observe that electromagnetic activity has a noticeable impact on the decrease of instability growth rate. Those plots show a relation between electromagnetic activity and the safety factor. When

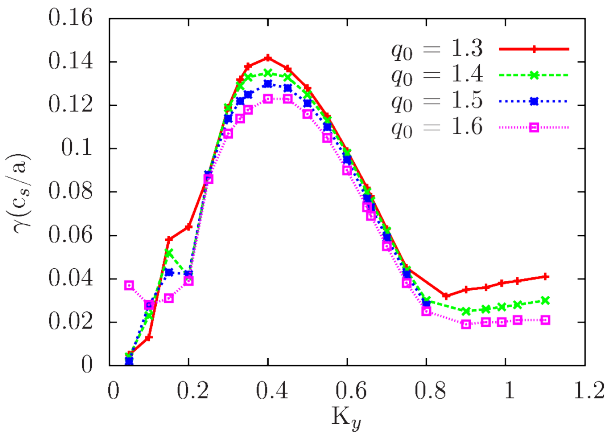

Fig. 5.5 Spectral analysis and safety factor scan for discharge 31563.

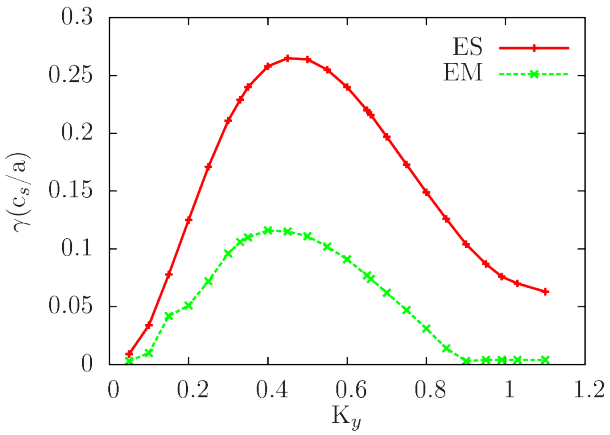

Fig. 5.6 Instability growth rate for a case with (green) and without (red) electromagnetic activity for discharge 31562.

high electromagnetic activity is taking place, the safety factor tends to degrade the instable modes at lower values, meanwhile electromagnetic activity alone stabilizes microinstabilities.

Together, the spectral analyses displayed in these figures point to a relative reduction of growth rate with high values of safety factor, fixed at 1.5 for our nonlinear simulations, and a reduction also due to electromagnetic effects alone.

Figure 5.8 shows the isolated impact of fast ions in stabilization. In this case, the safety factor was fixed at 1.5 and electromagnetic effects are taken into account. The safety factor choice gives a margin with a low value of growth rate, and at the same time it is KBM stable.

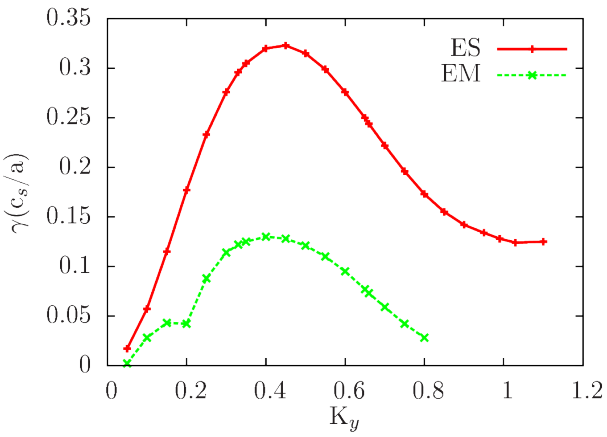

Fig. 5.7 Instability growth rate for a case with (green) and without (red) electromagnetic activity for discharge 31563.

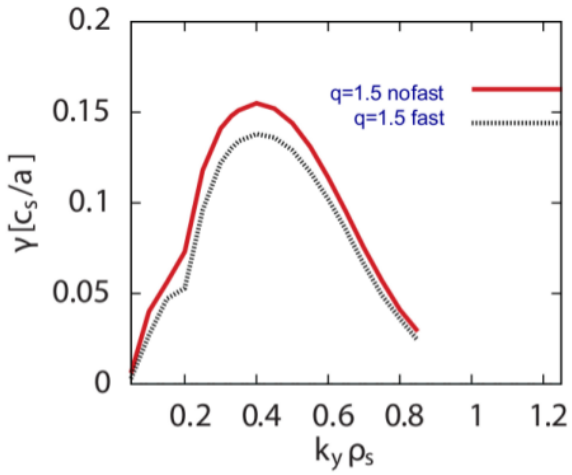

Fig. 5.8 Instability growth rate for a case with and without fast ions for discharge 31563.

5.2.2 Nonlinear results

To accurately study the stabilizing effect of fast ions, we carry out nonlinear GENE simulations. In this analysis, we focus on understanding the impact of fast ions in the main ion heat flux reduction and in the improvement of zonal shearing rate. These parameters give a quantitative insight in the stabilization of microturbulent activity.

Analysis of fluctuation contours and zonal flows

As a first approach, we analyze the impact of fast ions on zonal flow activity. As discussed in section 3.6.5, the zonal flow is the flow of plasma within a flux surface in the poloidal direction. It is localized in their radial extent transverse to the magnetic surfaces and it is a self-organized phenomenon driven by drift-type modes. The energy is transferred to longer wavelengths by modulational instability or turbulent inverse cascade [29].

Figure 5.9 shows the electric potential in the x and y plane. The value of the electric potential is given in terms of GENE normalized units. Here, we used a perpendicular domain size of $143\rho_s x 128\rho_s$ in x and y, with a grid of $(256x128x24x32x12)$ in $(x, y, z, v_{\|}, \mu)$ phase space.

With the zonal flow diagnostic tool, GENE allows to measure the time-averaged zonal shearing rate, which is 0.74 c_s/L_{ref} for the case without fast ion. The average zonal shearing rate is defined as $\left\langle K_x^2 \phi_{zf} \right\rangle$, where ϕ_{zf} is the zonal flow amplitude, and K_x is the wave number in the x direction.

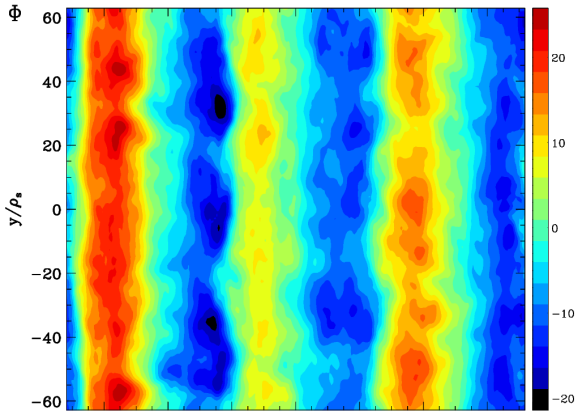

Fig. 5.9 The electric potential fluctuation levels for the case without fast ions of discharge 31563 in the x and y plane.

When analyzing the simulations including fast ions, we first observe that the contour flow of figure 5.10 is visually more ordered than in the case without fast ions. This observation is confirmed when the time-averaged zonal shearing rate is computed yielding a value of 0.94 c_s/L_{ref}, an increase of almost 30 %.

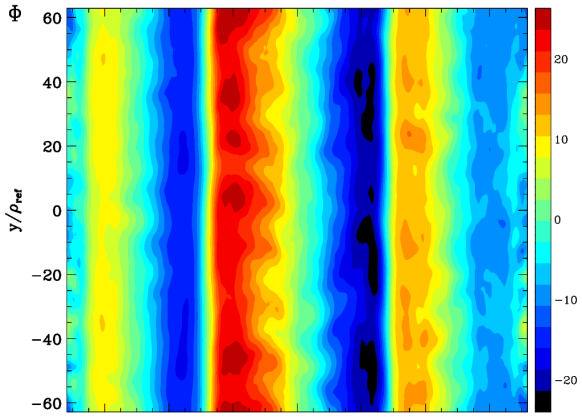

Fig. 5.10 The electric potential fluctuation levels for the fast ions case of discharge 31563 in the x and y plane.

The increase in the time-averaged zonal shearing rate indicates that fast ions may be playing a role in the stabilization of microturbulence by increasing the zonal flow, and therefore tearing the microturbulence modes, thereby reducing the radially outward flux.

In the case studied here, the zonal flow level saturates at a given amplitude, and because the fast ions can heat the deuterium directly through collisions, the instability growth rate is lower and the zonal flows shear apart the ITG eddies more easily.

Different factors play a role in the high value of central ion temperature, as discussed in chapter 3. In the present work, we are interested whether the fast ions have an impact on the stabilization of microturbulence rather than the diluting the main ions and directly coupling to the potential fluctuations, which in this case also reduces the growth rate. We are looking for a direct form of microturbulence stabilization.

To further understand the impact of fast ions on the main ion temperature increase reported in chapter 2, one needs to understand not only the instability growth rate behavior, but also the main ion heat flux.

Heat flux analysis

Nonlinear GENE simulations allow for the simulation of the heat fluxes and for the comparison between them and those obtained by power balance analysis of the experiment. In order to access the impact of fast ions in ITG microturbulence, emphasis will be given to

the ion heat flux. Because the electron heat flux level is smaller than the ion heat flux, and because the present work is focused on ion impact, we leave the electron analysis and the full transport analysis for a further study.

In discharge 31563, the experimental integrated ion heat flux at the radial position $\rho_{tor} = 0.25$ was deduced from the modeling of NBI with TRANSP and ICRH heating with FIDO and PION. It was found that the experimental ion heat flux is 1.6 MW.

To compare this value with GENE nonlinear simulations, we make a statistical time-average ion heat flux using one of GENE's diagnostic tool. In figure 5.11 we can see the ion flux levels for the simulation without fast ions. In this case, the statistical time-average ion heat flux given was of about 4.5MW.

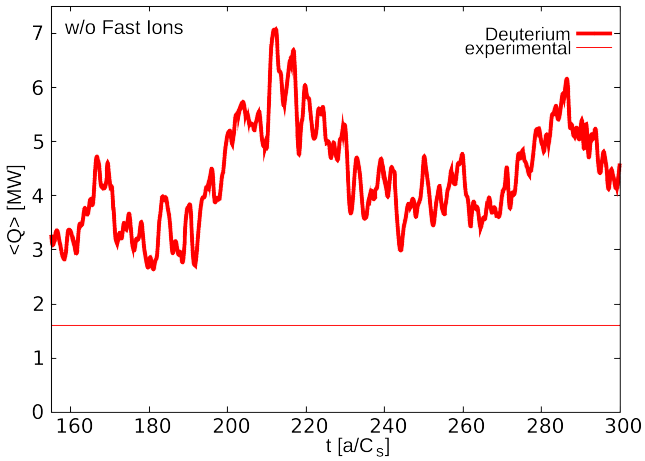

Fig. 5.11 Ion heat flux simulation for discharge 31563, the read horizontal line represents the experimental ion heat flux. The time is expressed in terms of GENE normalized units, which is approximately one microsecond.

The nonlinear ion heat flux simulations for the case with fast ions are seen in figure 5.12, and they give us values lower than experimental values, of about 1.3 MW. The heat flux level from GENE is 1.3, somewhat lower than the experiment. Nevertheless, small increases in the driving gradients are expected to yield a better agreement. A solution for this overestimation is presented in the next chapter.

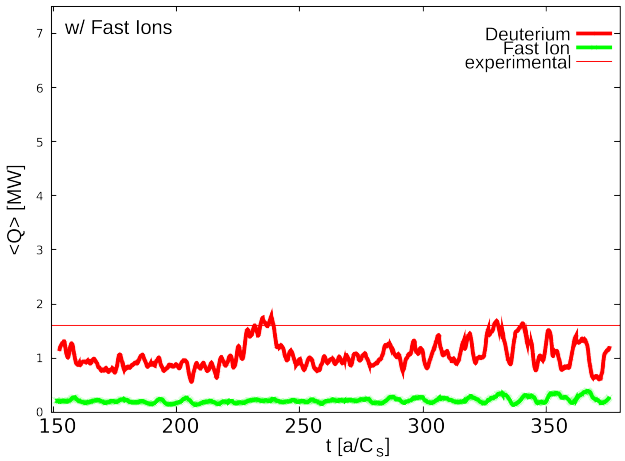

Fig. 5.12 The ion heat flux level for the simulation with fast ions is smaller than that in Fig 5.11, which is an indication of the stabilization of fast ions. The time is expressed in terms of GENE normalized units. The whole time interval corresponds to approximately one microsecond.

5.2.3 Beyond dilution and stabilization

The exact mechanism in which the stabilization takes place is not completely understood, but a few important conclusions can be made. One relevant point must be first considered, the dilution effect.

Dilution is a process in which the fast ions set the background thermal temperature to the experimental value. It reduces the n_i and a/L_n according to quasineutrality, while not considering fast ions in the dynamics. It happens only if $T_f >> T_i$. This effect is not reproduced in GENE. However, high values of fast ions density are needed [11] for dilution to take place. In our case, n_{fi}/n_e is around 5%. The low fast ion density discards, therefore, the possibility of dilution effects.

Having discarded the dilution effect, we are in the realm of beyond dilution stabilization. An interesting aspect of this effect is that we observe an active stabilization of microturbulence. In this case, the fast ion temperature reach a value in which the drift resonance falls into a region of the phase space where the fast ions take energy from the Ion Transport Gradient wave, instead of driving the increase of the instability.

In steady state the temperature is determined by the relation

$$S = D \cdot \nabla T. \tag{5.1}$$

Here S is the source, D is proportional to the diffusivity and T is the temperature. We observe that the gradient increases when we add ICRH source. The final gradient is very steep so we expect also a decreased transport coefficient, i. e. diffusivity. The source is collisional heating of the background F_0 in δf approaches, this is not solved in GENE where the transport coefficient and effect of fast ions are computed instead.

The mode is stabilized by increasing the ion pressure gradient, at constant electron temperature and density gradient. It is important to notice that in chapter 2, the relative electron temperature and density constancy was also experimentally reported. If the relative value of fast ion pressure is enough, a high value of local α_{MHD} is reached, where ITG modes are stable and no other instable modes are generated.

To summarize, the active stabilization of microturbulence due to fast ions has multiple reasons. It affects both the plasma geometry, through curvature reduction, and augmenting the local α_{MHD} parameter, as seen in section 3.2.1. It also generates a higher local pressure gradient, which is connected with stabilizing factors apart of its impact in α_{MHD} behavior. It affects the gradient of the temperature, just after the ICRH are turned on, and increase the pressure. All of those changes account for the stabilization of ITG modes. We conclude that in our case, ICRH driven fast ions do have an impact in the ITG instability growth rate beyond dilution. They can explain the high values measured in the experiments reported in chapter 3, and are a good candidate to trigger ITBs in further experiments.

Chapter 6

Conclusion

The objective of the present work was to analyze whether ICRH driven fast ions have an impact on the stabilization of microturbulences in two specific ASDEX Upgrade discharges. In order to understand the problem, we reviewed the experimental set up and established how the fast ions could be affecting the plasma.

It was noticed that changes in the plasma transport indicate a relation between the fast species and the plasma transport properties. A review of the plasma transport literature was done, and important relations between the particles distribution functions and transport properties were pointed out. To approach the problem, we used two numerical tools, FIDO and GENE. In the description of the tools, the relations between the particles distribution function and the transport properties were outlined.

We have shown in a linear GENE analysis that fast ions decrease the instability growth rate of Ion Temperature Gradient (ITG) modes. We have demonstrated also that due to the high electromagnetic nature of those experiments, microturbulence is further reduced due to the scaling with the safety factor.

In a nonlinear analysis, we demonstrated that the presence of fast ions significantly decreases the ion heat flux, which is an indicative of the increased central ion temperature measured in the experiment and described in chapter 2. Different of past findings, our results point towards a beyond dilution fast ion stabilization in which the effects are mostly noticed in nonlinear numerical simulations, and in which the in-depth stiffness of ion heat flux and gradient of ion temperature analysis is replaced by the safety factor and contour flux analysis.

We conclude that fast ions do have an impact on the stabilization of ITG microturbulence for the discharges in consideration. Nonetheless, other parameters such as electromagnetic activity also play a major role in the stabilization process.

In order to overcome the underestimation observed in the nonlinear heat flux analysis, this work could be further improved by including a more realistic fast ion distribution function such as a Bi-Maxwellian, which is a recent feature in GENE [30]. Besides small gradient increases, the introduction of such modification in the fast ion distribution could bring the ion heat flux values even closer to the experimental levels.

Another interesting improvement in the work would be related to the safety factor profile in FIDO. Instead of generating a profile with an internal algorithm, a subroutine could be created in order to read the experimental safety factor profile, or reconstruction profile. This would allow us to generate a more realistic fast ions density, temperature and pressure profile, which may lead to improved agreement with experimental results.

References

[1] S. Atzeni and J. Meyer ter Vehn. *The Physics of Inertial Fusion: Beam Plasma Interaction, Hydrodynamics, Hot Dense Matter*. Oxford, 2004.

[2] D. Gallart. *Computational Analysis of Ion Cyclotron Resonance Frequency Heating for DEMO*. PhD thesis, Universitat Politècnica de Catalunya, Barcelona, Spain, 2016.

[3] M. J. Mantsinen et al. Bulk ion heating with icrh waves in tokamaks. *AIP Conference Proceedings*, 1689(1):030005, 2015.

[4] K. Itoh P. H. Diamond, S.I. Itoh and T. S. Hahm. Zonal flows in plasma—a review. *Plasma Physics and Controlled Fusion*, 47(5):R35, 2005.

[5] J. R. Lamarsh and A. J. Baratta. *Introduction to Nuclear Engineering*. Pearson, 2001.

[6] J. D. Lawson. Some criteria for a power producing thermonuclear reactor. *Proceedings of the Physical Society*, Section B:70(1):6, 1957.

[7] J.P. Brasselet. *Vector fields on Singular Varieties*. Springer, 2009.

[8] www.iter.org.

[9] J Wesson. *Tokamaks*. Oxford University Press, 3rd edition, 2004.

[10] J. Citrin et al. Electromagnetic stabilization of tokamak microturbulence in a high-beta regime. *Plasma Physics and Controlled Fusion*, 57:014032, 2015.

[11] G. Tardini, J. Hobirk, V.G. Igochine, C.F. Maggi, P. Martin, D. McCune, A.G. Peeters, A.C.C. Sips, A. Stäbler, J. Stober, and the ASDEX Upgrade Team. Thermal ions dilution and itg suppression in asdex upgrade ion itbs. *Nuclear Fusion*, 47(4):280, 2007.

[12] M. Brambilla and R. Bilato. *Nuclear Fusion*, 49:085004, 2009.

[13] L.-G. Eriksson and T. Hellsten. *Phys. Scripta*, 55:70, 1995.

[14] J. Citrin et al. Nonlinear stabilization of tokamak microturbulence by fast ions. *Physical Review Letters*, 111:155001, 2013.

[15] J. Garcia et al. *Nuclear Fusion*, 55:053007, 2015.

[16] L. Vlahos T. Görler F. Jenko M. Mavridis, H. Isliker and D. Told. A study of self organized criticality in ion temperature gradient mode driven gyrokinetic turbulence. *Physics of Plasmas*, 21(10):102312, 2014.

[17] C. Bourdelle, G.T. Hoang, X. Litaudon, C.M. Roach, T. Tala, for the ITPA Topical Group on Transport, ITB Physics, and the International ITB Database Working Group. Impact of the alpha parameter on the microstability of internal transport barriers. *Nuclear Fusion*, 45(2):110, 2005.

[18] S. Havlin and D. ben Avraham. *Diffusion and Reactions in Fractals and Disordered Systems*. Cambridge University Press, 2000.

[19] H. Matsumoto K. McGuire W. A. Peebles Ch. P. Ritz P. W. Terry A. J. Wootton, B. A. Carreras and S. J. Zweben. Fluctuations and anomalous transport in tokamaks. *Physics of Fluids B: Plasma Physics*, 2(12):2879–2903, 1990.

[20] H. Sugama and W. Horton. Nonlinear electromagnetic gyrokinetic equation for plasmas with large mean flows. *Physics of Plasmas*, 5:2560, 1998.

[21] J.W. Connor. Magnetic confinement theory summary. *Nuclear Fusion*, 45(10):S1, 2005.

[22] F Romanelli and S Brigugli. Toroidal semicollisional microinstabilities and anomalous electron and ion transport. *Physics of Fluids B: Plasma Physics 2*, (4):754–763, 1990.

[23] F. Jenko, W. Dorland, M. Kotschenreuther, and B. N. Rogers. Electron temperature gradient driven turbulence. *Physics of Plasmas*, 7(5):1904–1910, 2000.

[24] T. Hellsten J. Carlsson and L.-G. Eriksson. *Proc. Joint Varenna Lausanne Workshop 'Theory of Fusion Plasmas'*, page 351, 1994.

[25] T. Hellsten L.-G. Eriksson and U. Willen. *Nuclear Fusion*, 33:1037, 1993.

[26] genecode.org.

[27] P. J. Mc Carthy. Analytical solutions to the grad–shafranov equation for tokamak equilibrium with dissimilar source functions. *Physics of Plasmas*, 6(9):3554–3560, 1999.

[28] F. Jenko, W. Dorland, and G. W. Hammett. Critical gradient formula for toroidal electron temperature gradient modes. *Physics of Plasmas*, 8(9):4096–4104, 2001.

[29] K. Itoh P. H. Diamond, S.I. Itoh and T. S. Hahm. Zonal flows in plasma—a review. *Plasma Physics and Controlled Fusion*, 47(5):R35, 2005.

[30] A. Di Siena et al. Zonal flows in plasma—a review. *J. Phys.: Conf. Ser.*, 775(012003), 2016.

Appendix A

Moments of the Boltzmann equation

A.1 Mass conservation

From the general framework exposed in chapter 3, one may derive important relations that are helpful to understand how transport takes place within the constrains of plasma physics, and how they related with the distribution function of the species. By firstly considering $\zeta = m$, where m is the mass of a given species, we have

$$\langle \zeta \rangle = m, \tag{A.1}$$

$$\langle \zeta v \rangle = m \langle v \rangle \equiv m\, \mathbf{u}, \tag{A.2}$$

and

$$\nabla_v \zeta = \nabla_v\, m = 0. \tag{A.3}$$

Replacing these quantities in the general transport equation we have

$$\frac{\partial \rho_m}{\partial t} + \nabla \cdot (\rho_m \mathbf{u}) = S. \tag{A.4}$$

Equation A.4 is known as the continuity equation. The term ρ represents the mass density $n \cdot m$, $\mathbf{u}$ is the linear velocity, and S represents the collision term.

By considering a collisionless scenario, dividing A.4 by the mass m, and multiplying the whole equation by the charge of the specie, one may arrive at the conservation of the electric charge equation

$$\frac{\partial \rho_q}{\partial t} + \nabla \cdot \mathbf{J} = 0. \tag{A.5}$$

Here, $\rho_q = n \cdot q$ is the charge density and $\mathbf{J} = \rho_q \mathbf{u}$ is the current density.

A.2 Momentum conservation

The conservation of momentum is extracted in a similar way as the mass conservation. Here, a more throughout analysis must be done in order to consider the standard variable $\zeta = mv$, being $v = w + u$, where w is the random movement around the mean velocity, and $\langle w \rangle = 0$.

Considering the acceleration in terms of the force and the mass, each of the terms can be reduced to

$$\frac{\partial}{\partial t}(n \langle \zeta(v) \rangle) = \frac{\partial}{\partial t}(m\, n\, u), \tag{A.6}$$

$$\nabla_v (m\, n \langle w_i w_j \rangle) = -\nabla \cdot \overleftrightarrow{\Psi}, \tag{A.7}$$

and

$$n \langle F \rangle = -n(r,t)\; q(E\; +\; v \times B). \tag{A.8}$$

Here, $\overleftrightarrow{\Psi}$ is the dyadic of pressure generated by the friction arising from the random movements w_i and w_j of the particles in different layers of the plasma. After considering the constrictions relative to the assumptions made, one will arrive at the following conservation equation

$$n\, m\, \frac{Du}{Dt} = n\, q\, (E + u \times B) - \nabla \cdot \overleftrightarrow{\Psi} - \delta. \tag{A.9}$$

This is the momentum conservation equation. It represents how the rate in change of momentum varies with the collision term δ, the internal pressure and the Lorentz forces.

A.3 Energy conservation

Following the treatment described in section 3.4.1, the energy transport equation can be extracted from the Boltzmann equation in a partial differential form. Here, the general

quantity ζ is replaced by the particle kinetic energy $\frac{mv^2}{2}$. In this case we have to consider the velocity as a two component quantity, and treat each term separately

$$\frac{\partial}{\partial t}(n\langle\zeta(v)\rangle) = \frac{\partial}{\partial t}(\frac{N\overleftrightarrow{\Psi}}{2} + \frac{m\,n\,u^2}{2}), \tag{A.10}$$

$$\nabla\cdot(n\langle\zeta(v)\rangle) = \nabla\cdot(Q(\frac{2+N}{2})\overleftrightarrow{\Psi}u + \frac{mnu^2}{2}u), \tag{A.11}$$

and

$$-n\langle a\cdot\nabla_v\zeta\rangle = -q\,n\,u\,\cdot E. \tag{A.12}$$

And the collision term is

$$\delta = -\left(\frac{\partial W}{\partial t}\right)_{coll}. \tag{A.13}$$

It represents the rate in which the energy is transferred among particles by collision effects.

Here, N represents the dimensional number in which the dyadic of pressure is considered, for isotropic cases it is considered unit. The quantity Q is the heat flux, expressed as

$$Q = \int_v \frac{mw^2}{2} w\, f\, d^3v. \tag{A.14}$$

Bringing up all the terms together and performing the necessary adjustments, we have

$$\frac{N}{2}\frac{D\overleftrightarrow{\Psi}}{Dt} + \frac{2+N}{2}\overleftrightarrow{\Psi}\nabla\cdot u = -\nabla\cdot Q + \delta\cdot u - (\frac{\partial W}{\partial t})_{coll}, \tag{A.15}$$

where $\delta\cdot u$ represents the heating due to friction processes, and $(\frac{\partial W}{\partial t})_{coll}$ the energy transferred by collision.

Appendix B

Random walk approach coefficients

Considering the random walk approach, the electron heat and particle fluxes are described as

$$D_{\perp e} = D_{\perp ei} \sim \nu_{ei}\rho_e^2, \tag{B.1}$$

and

$$\chi_{\perp e} = \chi_{\perp ee} + \chi_{\perp ei} \sim (\nu_{ee} + \nu_{ei})\rho_e^2. \tag{B.2}$$

And for the ions we have a similar situation,

$$D_{\perp i} = D_{\perp ei} \sim \nu_{ei}\rho_e^2, \tag{B.3}$$

and

$$\chi_{\perp i} = \chi_{\perp ii} + \chi_{\perp ie} \sim \nu_{ii}\rho_i^2. \tag{B.4}$$

It is easy to observe that since $D_{\perp e} = D_{\perp i}$, the perpendicular transport is ambipolar, and no charge separation is generated.

Parallel to B, in a similar way, the transport coefficients can also be determined. We must consider here that the step size is related to the mean free path of the particle, $\lambda = \frac{v_T}{\nu}$, consequently, for the electron-electron case

$$\chi_{\parallel ee} \sim \nu_{ee}\lambda_e^2 \sim \frac{v_{Te}^2}{\nu_e}, \tag{B.5}$$

and

$$D_{\parallel ee} = 0. \tag{B.6}$$

For the ion-ion case

$$\chi_{\parallel ii} \sim \nu_{ii}\lambda_i^2 \sim \frac{v_{Ti}^2}{\nu_i}, \tag{B.7}$$

and

$$D_{\parallel ii} = 0. \tag{B.8}$$

The electron-ion case is expressed as

$$\chi_{\parallel ei} \sim \nu_{ei}\lambda_i\lambda_e \sim \frac{v_{Ti}^2}{\nu_i}, \tag{B.9}$$

and

$$D_{\parallel ei} \sim \frac{v_{Ti}^2}{\nu_i}. \tag{B.10}$$

We also have for electrons

$$D_{\parallel e} = D_{\parallel ei} \sim \frac{v_{Ti}^2}{\nu_i}, \tag{B.11}$$

and

$$\chi_{\parallel e} \sim \nu_e\lambda_e^2. \tag{B.12}$$

And for ions

$$D_{\parallel i} = D_{\parallel ei} \sim \frac{v_{Ti}^2}{\nu_i}, \tag{B.13}$$

and

$$\chi_{\parallel i} \sim \nu_{ii}\lambda_i^2. \tag{B.14}$$

Observe that, for a first order approximation where ions and electrons have the same temperature, perpendicular transport is highly dominated by ion heat diffusion, but the parallel transport is, differently, dominated by electron heat diffusion. The parallel heat transport, in this scenario, can be up to thousands times larger than perpendicular heat transport.

Appendix C

First approximation to neoclassical flux

If we consider the balance equations, with a gradient of the temperature equals zero and $E = E^A - \nabla\phi$, we are capable of determining flows characteristic to classical transport and its coefficients for magnetized plasmas.

From the electron entropy relation, we can arrive in the following relation

$$mn\frac{dV}{dt} = nq(E^A - \nabla\phi + V \times B) - \nabla p - \nabla\cdot\Pi - nq\left(\frac{J_\parallel}{\sigma_\parallel} + \frac{J_\perp}{\sigma_\perp}\right). \tag{C.1}$$

From the above equation, a perpendicular, parallel and cross component to the flow is extracted. The parallel flow is determined by

$$mn\frac{dV_\parallel}{dt} = nq(b\cdot E^A - b\cdot\nabla\phi) - b\cdot\nabla p - b\cdot\nabla\cdot\Pi - nq\frac{J_\parallel}{\sigma_\parallel}. \tag{C.2}$$

Consider b to be equal to $\frac{B}{|B|}$. The $E\times B$ and diamagnetic flows are retrieved as a first order approximation of the perpendicular flows. For a first order perturbation approximation of ϕ, the electric potential, and p, the pressure, one has

$$V_{\perp,1} = \frac{1}{B^2}B\times\left(\nabla\phi_0 + \frac{1}{nq}\nabla p_0\right), \tag{C.3}$$

and

$$J_{\perp,1} = \sum nqV_{\perp,1} = \frac{1}{B^2}B\times\nabla(p_e + p_i). \tag{C.4}$$

The equations of the perpendicular transport flows are extracted from the perpendicular components in higher orders

$$V_{\perp,2} = \frac{1}{nqB^2} B \times (mn\frac{dV_\perp}{dt} + \nabla \cdot \Pi + \frac{nq}{\sigma_\perp} J_{\perp,1}) + \frac{1}{B^2} B \times (\nabla \phi_1 + \frac{1}{nq} \nabla p_1) + \frac{1}{B^2} E^A \times B. \quad \text{(C.5)}$$

Here, the sum of the second, forth and fifth terms of the right hand side give us coefficients related to neoclassical transport, and the third is related to classical transport. The last term is related to grid velocity. The pressure is

$$J_{\perp,2} = \frac{1}{B^2} B \times \left(\rho_m \frac{dV_{\perp,i}}{dt} + \sum_s \nabla \cdot \Pi_s + \nabla \sum_s p_{1,s} \right). \quad \text{(C.6)}$$

In the classical transport due to friction between diamagnetic flows the classical diffusion is equal to $D_{cl} \nabla \ln n$, where $D_{cl} = \frac{T_e + T_i}{2T_e} \nu_e \rho_e^2$.

From the balance equations, a peculiar set of equations with important characteristics are extracted. Consider an axisymmetric geometry, where

$$B = I \nabla \zeta + \nabla \zeta \times \nabla \Psi, \quad \text{(C.7)}$$

and

$$\frac{\nabla \Psi \times B}{B^2} = -I \frac{B}{B^2} + R^2 \nabla \zeta. \quad \text{(C.8)}$$

In a tokamak geometry, consider also that the axisymmetric condition bring us the following considerations

$$\langle A \rangle \equiv \frac{\oint \frac{dl}{B} A(l)}{\oint \frac{dl}{B}}, \quad \text{(C.9)}$$

and

$$\langle B \cdot \nabla f \rangle = 0. \quad \text{(C.10)}$$

From the parallel momentum balance, expressed in equation C.2, we have

$$0 = nq(B \cdot E^A - B \cdot \nabla \phi_1) - B \cdot \nabla p_1 - B \cdot \nabla \cdot \Pi - nq \frac{J_\parallel B}{\sigma_\parallel}. \quad \text{(C.11)}$$

The particle flux can be reduced to

$$\Gamma_\Psi \equiv \left\langle V_{\perp,2} \cdot \nabla \Psi \right\rangle. \quad \text{(C.12)}$$

Considering the description of $V_{\perp,2}$ here exposed, one may arrive in the following relations

$$\Gamma_{\Psi}^{neo} = -\frac{I}{q}\left\langle \frac{1}{B^2}\left[nq(B\cdot\nabla)\phi_1 + (B\cdot\nabla)p_1 + B\cdot\nabla\cdot\Pi\right]\right\rangle \tag{C.13}$$

$$= nI\left\langle\left(\frac{1}{B^2} - \frac{1}{\langle B^2\rangle}\right)\left(\frac{J_{\parallel}B}{\sigma_{\parallel}} - E_{\parallel}^{A}B\right)\right\rangle + \frac{nI}{\langle B^2\rangle}\left\langle\frac{J_{\parallel}B}{\sigma_{\parallel}} - E_{\parallel}^{A}B\right\rangle. \tag{C.14}$$

The first bracket represents the Pfirsch-Schlüter transport, within the flux surface, and the second one, averaging the flux surface, the Banana-Plateau.

The total current within the flux surface, considering the charge continuity equation, is found to be

$$J_{\parallel}B = -I\frac{d}{d\Psi}(p_e + p_i)(1 - \frac{B^2}{\langle B^2\rangle}) + \frac{\langle J_{\parallel}B\rangle B^2}{\langle B^2\rangle}. \tag{C.15}$$

The first term in the right hand side is the Pfirsch-Schlüter current, resulting in a diffusive flux $\Gamma^{PF} \sim q^2(\Psi)D_{CL}$ and larger than the classical diffusion values.